RSC Advances

ROYAL SOCIETY OF CHEMISTRY

REVIEW

View Article Online
View Journal | View Issue

Check for updates

Cite this: *RSC Adv.*, 2025, **15**, 36179

Mechanistic insights on CO_2 fixation *via* electrochemical and photocatalytic reduction

Sawaira Altaf,[a] Tanveer Hussain Bokhari*[a] and Muhammad Bilal *[ab]

The electrochemical and photochemical conversion of CO_2 into value-added chemicals and fuels has emerged as a sustainable approach to mitigate climate change and provide renewable energy carriers. Recent advances span heterogeneous and homogeneous catalysts, single- and dual-atom alloys, and MOF-derived materials, each offering unique opportunities to enhance activity, selectivity, and durability. Heterogenized molecular catalysts, such as $Re^{(I)}$, $Mn^{(I)}$, and $Ru^{(II)}$ complexes on TiO_2, demonstrate site isolation that suppresses dimerization and side reactions, thereby improving product selectivity toward CO, formate, or syngas. Single-atom alloys (SAAs) and dual-atom catalysts (DACs) exploit synergistic electronic and geometric effects to tune the adsorption energies of key intermediates, enabling efficient formation of C_1 and C_{2+} products, including CH_4, CH_3OH, and ethylene. MOF-derived electrocatalysts offer high surface areas, tunable pore environments, and adjustable active sites, promoting CO_2 adsorption, activation, and multielectron reduction. Photocatalytic systems benefit from optimized light absorption, efficient charge separation, and surface site engineering to drive selective CO_2 reduction under visible light. Integrating mechanistic insights with rational design principles, such as electronic structure modulation, heterogenization, and cooperative bimetallic interactions, provides a framework for developing next-generation CO_2 reduction catalysts with enhanced selectivity, turnover, and durability. This review highlights recent progress and mechanistic understanding.

Received 1st July 2025
Accepted 13th September 2025

DOI: 10.1039/d5ra04681e

rsc.li/rsc-advances

1. Introduction

The urgent need to transition from fossil fuels to renewable energy stems from escalating human-driven carbon dioxide

---

[a] Department of Chemistry, Government College University Faisalabad, 38000, Pakistan. E-mail: tanveer.bokhari@yahoo.com; muhammadbilalgcuf@gmail.com
[b] Higher Education Department, Lahore, 54000, Punjab, Pakistan

Sawaira Altaf

Sawaira Altaf obtained her Bachelor's degree from the Government College University, Faisalabad, under the supervision of Prof. Dr Tanveer Hussain Bokhari. Her research interests focus on organometallic chemistry, CO_2 fixation, and the hydrogen evolution reaction.

Tanveer Hussain Bokhari

Dr Tanveer Hussain Bokhari obtained his PhD degree in Chemistry from GC University, Lahore, after being awarded with the Indigenous Scholarship for PhD by the Higher Education Commission Islamabad. He did his postdoctoral studies at Brigham Young University, USA. He has published 160 research papers at international and national levels in well-reputed journals and is the author of two books. Currently, he is serving as a Professor of Chemistry at the Department of Chemistry, Government College University Faisalabad, where he was awarded the Research Productivity Award twice in 2011 and 2012 by the Pakistan Council for Science and Technology, Islamabad-Pakistan. His research interest focuses on organometallic chemistry.

levels in the atmosphere. To resolve this imbalance, surplus renewable electricity or direct solar energy can be harnessed to convert CO_2 into liquid fuels *via* electrolysis or photolysis.[1–10] Photocatalytic CO_2 reduction pioneered through semiconductor-based systems uses sunlight to trigger reactions that transform CO_2 into fuels.[11–15] Meanwhile, electrochemical methods leverage renewable electricity to convert captured CO_2 emissions into industrial feedstocks.[16–18] Both pathways aim to close the carbon cycle by turning CO_2 into value-added products.[19–22] Designing catalysts that drive the multi-proton, multi-electron reduction of CO_2 (CO_2RR) is crucial for transforming CO_2 into useful single-carbon compounds, such as formic acid, carbon monoxide, formaldehyde, methanol, and methane. A major obstacle lies in addressing the substantial energy hurdles tied to activating CO_2, which must be lowered to allow the reaction to proceed efficiently at moderate voltages while maintaining precise control over the desired products.[23–27]

The enthalpy of formation for carbon dioxide, a nonpolar molecule in which carbon exhibits a +4 oxidation state, is -394.38 kJ mol^{-1}, reflecting its high thermodynamic stability. Capturing and converting CO_2 generally demands considerable energy input, often involving elevated pressures or catalytic assistance. Current CO_2 fixation strategies primarily include electrochemical,[28] thermochemical,[29–31] photocatalytic[32–34] and biological[35–37] approaches. Among these, the thermochemical route typically involves high-temperature hydrogenation processes to enable the transformation and utilization of CO_2 *via* complex multistep reactions.[38] However, this method suffers from a low energy utilization rate and achieves a conversion efficiency of merely 0.7–0.8%.[39]

Photocatalytic chemical fixation stands out due to its mild operating conditions, environmental compatibility, diverse product range, and high yields, making it a highly promising and ideal method.[40–44] In 1979, Inoue and colleagues reported the use of semiconductor photocatalysts such as TiO_2, ZnO, GaP, CdS and SiC suspended in CO_2-saturated water, where CO_2 was successfully reduced under ambient conditions to produce hydrocarbons.[45] This pioneering work sparked widespread interest in photocatalytic CO_2 conversion. Utilizing solar energy and semiconductor photocatalysts, this approach enables the direct transformation of CO_2 into hydrocarbon fuels at room temperature and atmospheric pressure. Given the abundance of raw materials and the sustainability of solar energy, this method is considered both environmentally benign and economically viable, offering a potential solution to both environmental pollution and energy shortages. Nevertheless, several challenges must be addressed for future industrial-scale application, particularly enhancing the efficiency of CO_2 fixation under natural sunlight and reducing the cost of photocatalysts and ligands.[46]

In the electrochemical fixation of CO_2, the primary pathway involves the electrochemical reduction of CO_2, which predominantly yields short-chain carbon products. Due to the complex nature of this process, which involves multiple electron-transfer steps, a variety of short-chain reduction products are typically formed. However, achieving direct CO_2 reduction on the electrode surface requires the application of a substantial overpotential, which significantly lowers the overall energy utilization efficiency. Many catalysts built from transition metals, which can effectively bind and reduce CO_2, become electron-rich when in their reduced state. While this property aids in CO_2 activation, it also enhances their tendency to promote the hydrogen evolution reaction (HER) (Fig. 1).[47–49] Here, protons sourced from water required for CO_2 reduction compete with CO_2 molecules, diverting the reaction toward hydrogen gas production. Additionally, the inherent complexity of CO_2 reduction pathways often leads to a mix of possible outputs, further complicating efforts to steer the selectivity toward a single target product. For example, the complete reduction of CO_2 *via* an $8H^+/8e^-$ pathway yields CH_4, while partial reductions produce intermediates such as CO or HCOOH ($2H^+/2e^-$), HCHO ($4H^+/4e^-$), or CH_3OH ($6H^+/6e^-$), alongside various C_2 and C_3 compounds (Scheme 1).[50–62]

One-carbon-containing compounds are predominantly sourced from petrochemical feedstocks. It represents a vital economic resource, which motivates ongoing research into catalytic systems capable of converting CO_2 into C_1-valuable products. Meanwhile, achieving selective CO_2 reduction remains a fundamental challenge. The viable CO_2RR must additionally withstand exposure to oxygen and common industrial byproducts such as sulfur and nitrogen oxides (SO_x or NO_x, respectively). This operational resilience is particularly essential for deploying CO_2 conversion technologies directly at heavy emission facilities which usually consume the fossil fuels. So, integrating such processes without costly CO_2 purification steps could significantly enhance feasibility.[63]

The electronic structure of CO_2 frontier molecular orbitals serves as a critical guide for engineering effective metal-based catalysts to drive its reduction. This framework facilitates the optimization of the electronic properties of the catalytic metal center and its coordination geometry, thereby promoting CO_2 conversion. Specifically, a metal center with an oxidation state of +1 or 0 and d^8 electron configuration stabilized in a square–pyramidal ligand has been shown to exhibit high efficiency in interacting with and activating the CO_2 molecule (Fig. 2). This is achieved through synergistic orbital interactions. The filled d_{z^2} orbital engages in σ-bonding, while the $d_{xz/yz}$ orbitals enable π back-bonding, collectively weakening the C=O bonds to drive reduction.[63,64]

Muhammad Bilal

Muhammad Bilal received his Bachelor's and Master's degrees from the Government College University, Faisalabad, under the supervision of Prof. Nasir Rasool. Then, he joined the Higher Education Department Pakistan as a Lecturer in Chemistry. Subsequently, he joined Shandong University as a PhD scholar. Currently, his research focuses on reactions involving electrochemistry or earth-abundant transition metals.

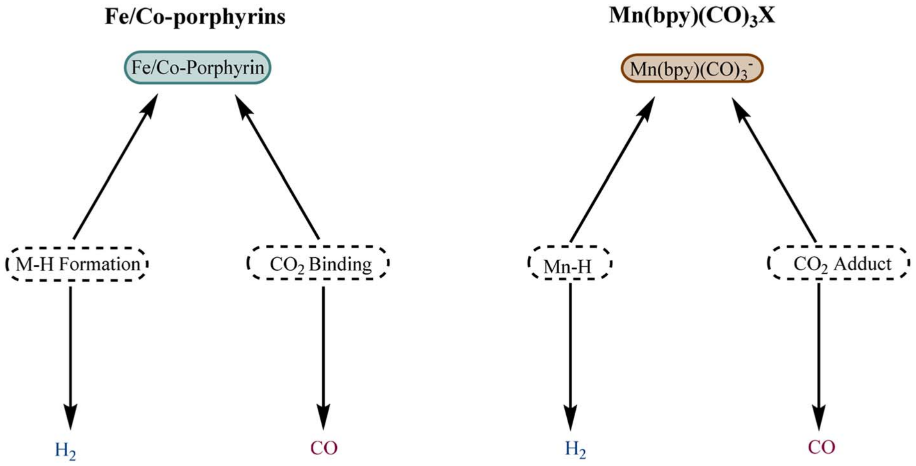

Fig. 1 CO$_2$ binding modulates the reaction pathways and facilitates the HER.

$$CO_2\,(aq) + e^- \longrightarrow CO^{-\bullet}\,(aq) \qquad E^\circ = -1.90\ V \quad (1)$$

$$CO_2\,(g) + 2H^+ + 2e^- \longrightarrow CO\,(g) + 2H_2O \qquad E^\circ = -0.52\ V \quad (2)$$

$$CO_2\,(g) + 2H^+ + 2e^- \longrightarrow HCOOH\,(aq) \qquad E^\circ = -0.6\ V \quad (3)$$

$$CO_2\,(g) + 4H^+\ 4e^- \longrightarrow HCHO\,(g) + H_2O \qquad E^\circ = -0.48\ V \quad (4)$$

$$CO_2\,(g) + 6H^+ + 6e^- \longrightarrow CH_3OH\,(aq) + H_2O \qquad E^\circ = -0.38\ V \quad (5)$$

$$CO_2\,(g) + 8H^+ + 8e^- \longrightarrow CH_4\,(g) + 2H_2O \qquad E^\circ = -0.24\ V \quad (6)$$

$$2H^+\,(aq) + 2e^- \longrightarrow H_2\,(g) \qquad E^\circ = 0\ V \quad (7)$$

$$O_2\,(g) + 4H^+ + 4e^- \longrightarrow 2H_2O \qquad E^\circ = 0.82\ V \quad (8)$$

Scheme 1 Summary of half-cell reactions.

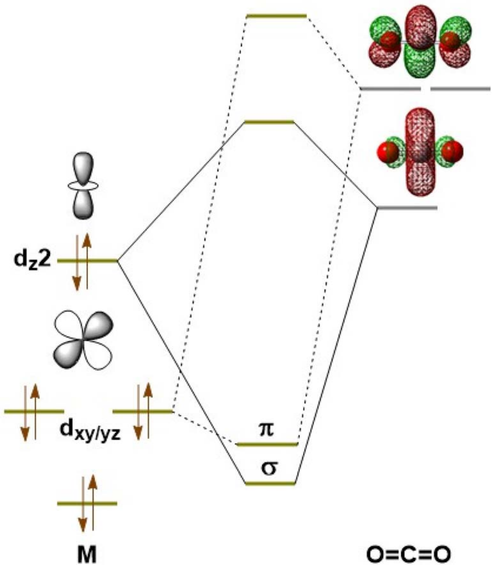

Fig. 2 Bonding between CO$_2$ and a d^8 metallic orbital.

Researchers have successfully engineered a range of high-performance catalysts tailored for converting carbon dioxide efficiently and with precise control.[65,66] Recent approaches include incorporating functional groups that act as hydrogen bond donors, local proton donors, or positively charged moieties to boost the catalytic performance.[67–74] The environment in the second sphere has led to a significantly higher rate of CO$_2$RR.[75–78] Enhancing selectivity has been achieved by stabilizing reaction intermediates through hydrogen bonding and controlled proton transfer.[75–77,79] Photocatalytic and electrocatalytic CO$_2$ reduction are two key methods for converting CO$_2$ into useful products. Photocatalysis harnesses solar energy, where semiconductors absorb light, generating electron–hole pairs that drive redox reactions on the surface. It operates under mild conditions but is limited by narrow light absorption, fast carrier recombination, and slow surface kinetics. Electrocatalysis uses an external electric field to drive CO$_2$ reduction at the cathode and oxidation at the anode, requiring conductive, corrosion-resistant materials with active sites. It offers faster rates and greater control. Photocatalytic systems need efficient light-transmitting reactors but face design trade-offs, while electrocatalytic systems depend on optimized electrodes, electrolytes, and membranes. Although photocatalysis has lower material costs, its low efficiency raises hydrogen production costs, whereas electrocatalysis, while efficient, requires affordable renewable electricity for sustainability.[61]

Reported review articles relatively tend to focus either on mechanistic details or specific factors affecting photocatalytic or electrochemical CO$_2$ reduction. Some reports highlight surface-science approaches such as MOF-based single-atom and dual-atom catalysts to improve C–C coupling and selectively produce valuable C$_{2+}$ products *via* catalyst design, crystal surface control, and bimetallic systems. In contrast, this article delves into mechanistic insights of CO$_2$ photochemical and electrochemical reduction, emphasizing the electronic structure, spin states, and ligand design in directing product selectivity. It also presents molecular-level perspectives and introduces MIOM hybrid systems to address challenges related to efficiency and stability. Together, these studies demonstrate the importance of integrating a mechanistic understanding with advanced catalyst and system design to enable practical

CO_2 conversion technologies. This review specifically focuses on the fundamental mechanistic principles governing catalytic CO_2 reduction, examining how key intermediates are identified and characterized through spectroscopic and spectroelectrochemical techniques, revealing the influence of their electronic structures on the catalytic performance. The literature covered in this article spans published reports up to March 2025.

2. Electrochemical CO_2RR

Carbon dioxide behaves as an amphoteric compound, with its carbon atom acting as a Lewis acid and its oxygen atoms functioning as Lewis bases. Its electron affinity is approximately −0.66 eV.[80–84] With a first ionization potential around 13.8 eV, CO_2 is more inclined to accept electrons than to donate them. This characteristic plays a key role in CO_2RR, where the electrophilic carbon atom is more reactive than the mildly nucleophilic oxygen atoms. CO_2 reduction generally follows one of two primary pathways, one of which involves insertion into a metal–hydride bond (pathway A) or binding directly to the catalyst metal center (pathway B) (Scheme 2).

2.1. CO_2 binding

The first step in CO_2 activation typically involves a nucleophilic attack by an electron-rich metal center on the electrophilic carbon of the CO_2 molecule (Scheme 2; Pathway B). In the CO_2 molecule, the highest occupied molecular orbital (HOMO) is primarily localized on the more electronegative oxygen atoms. The lowest unoccupied molecular orbital (LUMO) is a C–O σ* antibonding orbital with substantial electron density concentrated on the carbon atom. Additionally, the next set of unoccupied orbitals (LUMO+1) consists of degenerate C–O π* orbitals both in plane and out of the plane (Fig. 1). To enable CO_2 reduction, electrons usually donated from the metal orbitals of the catalyst must fill the σ* and π* orbitals of the CO_2 molecule. Successful activation relies on the presence of filled d_{z^2} and $d_{xz/yz}$ orbitals at the metal center that are well-suited to interact with the target CO_2 orbitals. Many complexes featuring a tetragonal ligand environment and d^8 configuration (Co^+, Fe^0 and Ni^{2+}) meet these criteria. Catalytic activity is also possible with species that have a half-filled d_{z^2} orbital, including Co^{2+} and Fe^+. Transition metal complexes from the second and third rows can exhibit similar behavior.[64,85] The interactions between metal complexes and CO_2, along with their binding constants, can be evaluated using cyclic voltammetry. When CO_2 quickly associates with a metal center during its reduction, a noticeable shift in the faradaic signal is often observed. However, in some cases, no such shift is observed. This can occur if the reduced metal species either does not react with CO_2 within the timescale of the CV experiment, or if the CO_2 binding affinity is too weak to produce a detectable change.[86]

Numerous M–CO_2 complexes have been documented in organometallic studies. Although these compounds may not directly participate in catalytic CO_2 reduction, they offer valuable insight into the spectroscopic characteristics typically associated with M–CO_2 bonding. M–CO_2 adducts are commonly analyzed using vibrational spectroscopy, as these species contain a prominent C=O chromophore that typically absorbs in the 1500–1800 cm^{-1} range of the near-infrared spectrum.[86–90] At −95 °C, these M–CO_2 complexes were formed through chemical methods by introducing CO_2 into a solution of $Fe^{(0)}$ porphyrin. A transient intermediate was observed under these conditions, exhibiting a half-life of less than 30 seconds at −95 °C, as identified by resonance Raman spectroscopy (Fig. 3A).[50] The C–Fe stretching vibration and OCO bending mode appeared at 590 cm^{-1} and 806 cm^{-1}, respectively. Both signals shifted to lower frequencies when ^{13}C-labeled CO_2 was used. Notably, the δ_{OCO} bending frequency closely matches the values typically seen when CO_2 is coordinated to metal surfaces.[91] Shifts were detected in the ν_4 and ν_2 bands of the porphyrin ligand, which are sensitive indicators of the metal oxidation and

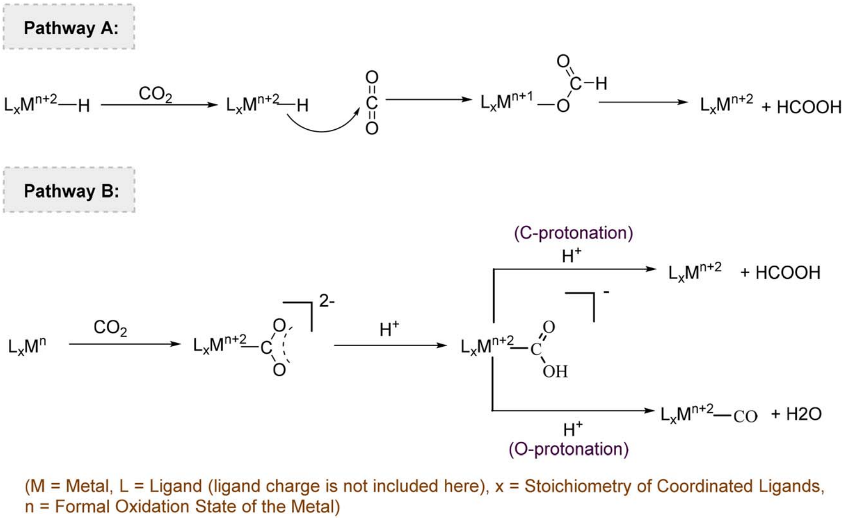

Scheme 2 Proposed routes for CO_2 reduction reactions.

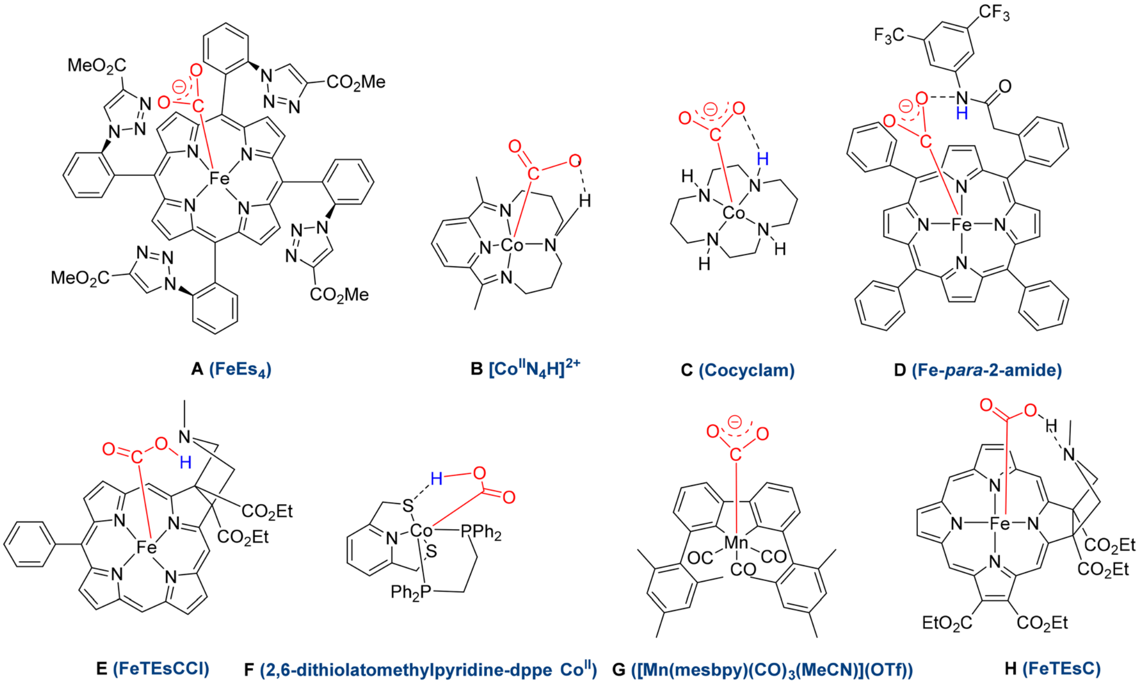

A (FeEs$_4$) **B [Co^{II}N$_4$H]$^{2+}$** **C (Cocyclam)** **D (Fe-*para*-2-amide)**

E (FeTEsCCl) **F (2,6-dithiolatomethylpyridine-dppe Co^{II})** **G ([Mn(mesbpy)(CO)$_3$(MeCN)](OTf))** **H (FeTEsC)**

Fig. 3 Spectroscopically identified metal–COOH or metal–CO_2 intermediates participating in CO_2 reduction reactions.

spin states, confirming that CO_2 binding converted Fe$^{(0)}$ to Fe$^{(II)}$. This corresponds to a 2-electron reduction of CO_2, producing an electronic configuration of Fe$^{(II)}$–CO_2^{2-}. A CoI–CO_2 intermediate has also been briefly detected during the photocatalytic reduction of CO_2 using a cobalt macrocycle, showing a CO stretching frequency at 1670 cm^{-1} (Fig. 3B).[92] In a separate study, a CoI–CO_2 adduct was identified through FTIR spectroscopy, with a CO_2 stretching frequency observed at 1544 cm^{-1} (Fig. 3C).

X-ray absorption spectroscopy results provided confirmation that Co$^{(I)}$ is oxidized to Co$^{(III)}$ when CO_2 is bound. A notable shift of the absorption edge to higher energy in the CO_2-bound Co$^{(I)}$ species pointed to the formation of a CO_2^{2-}-bound Co$^{(III)}$ species, which results from the transfer of 2e$^-$ from the cobalt center to the coordinated carbon dioxide molecule.[86] CO_2 binding is enhanced when the extra negative charge is stabilized by a nearby Lewis acidic metal center, as well as through electrostatic interactions and hydrogen bonding.[93,94] A recent study emphasized the importance of placing second-sphere donors. Positional isomers, *ortho* or *para* with pendant amide groups, are located either close to or farther from the active site. The study revealed that placing second-sphere donor groups at the *ortho* position, while maintaining a greater distance between the hydrogen bond donor and the metal center, markedly improves the rate of CO_2 reduction. This distal *ortho* arrangement allows the molecule to adopt a shape that promotes H-bonding and eases H$^+$ transfer to the metal–CO_2 complex (Fig. 3D).[95] Recently, the Dey group reported an iron chlorin species featuring a pendant amine group in its secondary coordination sphere (Fig. 3H), which typically catalyzes CO_2 reduction to formic acid with low overpotential from its Fe$^{(I)}$ state, which is also capable of driving CO_2 reduction from its Fe$^{(0)}$ state, producing methanol as the primary product with a faradaic efficiency of about 50%.[96] The Zhang group validated Dey's findings through computational studies. Their calculations are in good agreement with experimental observations that the formal Fe$^{(I)}$–porphyrin would directly bind with a CO_2 molecule to trigger a 2e$^-$ reduction of CO_2. The unusual behavior could be ascribed to the significant hydrogen bonding and through-space electrostatic attractions between the cationic N–H terminal and the CO_2-adduct. The electronic structure of the formal Fe$^{(I)}$–porphyrin should be better demonstrated as Fe$^{(II)}$–Por$^{\bullet-}$, which incorporates a ferrous center and a 1e$^-$ reduced porphyrin ligand. The key Fe$^{(III)}$–COOH and Fe$^{(II)}$–COOH intermediates were investigated, which demonstrated that the cationic N–H would generate an H-bond with the O-terminal of the carbonyl of the COOH moiety. The significant H-bonds, as well as through-space electrostatic attraction, would facilitate the subsequent C-protonation to yield HCOOH. In addition, the cationic N–H terminal is found to hinder the dissociation of CO. The computational results adequately elucidate the origins of HCOOH selectivity over CO, and, more importantly, provide an insightful mechanistic understanding of the cooperative roles of second-sphere hydrogen bonding and cationic effects.[97]

Enhanced electrochemical CO_2 reduction observed with iron porphyrins bearing H-bonding functionalities is attributed to the stabilization of the CO_2-bound intermediate through a combination of electrostatic interactions and H-bonding, as supported by DFT studies. When CO_2 binds to the reduced state, it forms an Mn^{2+}–CO_2^{2-} intermediate. This species, due to its high basicity, is easily protonated by weak acids, leading to the formation of a metal carboxylate complex. The initial protonation step is particularly favorable, as the Mn^{2+}–CO_2^{2-}

intermediate has a pK_a higher than that of methanol, making it highly susceptible to proton transfer. An example of this behavior is observed with the Fe^{2+}–CO_2^{2-} complex. The enhanced rate of electrochemical CO_2 reduction observed with iron porphyrins that contain hydrogen-bonding groups is believed to stem from the stabilization of the CO_2-bound intermediate. This stabilization arises through hydrogen bonding and electrostatic interactions, as suggested by DFT studies. When CO_2 binds to the reduced metal center (Mn), it forms a Mn^2–CO_2^{2-} complex. Due to the high basicity of this intermediate (with a pK_a higher than that of methanol), it readily undergoes protonation by weak acids, producing a metal–carboxylate species.

This initial protonation step is particularly favorable because of the strong basic character of the Mn^{2+}–CO_2^{2-} species. For instance, in reactions where CO_2 is captured by an $Fe^{(0)}$–porphyrin complex, an $Fe^{(II)}$–CO_2^{2-} intermediate forms and is easily protonated by mild acids such as methanol or phenol. This yields an $Fe^{(II)}$–COOH species which can be identified by characteristic vibrational markers, specifically the porphyrin ν_4 and ν_2 bands, which indicate a low-spin $Fe^{(II)}$ state. Additional spectroscopic signals include a C–OH stretch at 1189 cm^{-1}, a C═O stretch at 1573 cm^{-1}, and Fe–C stretch at 521 cm^{-1}. These assignments are confirmed through isotopic labeling with ^{13}C and ^{2}H. Among the steps in this CO_2 reduction process, the final protonation leading to carbon monoxide formation is the slowest under the studied conditions. The low-spin COOH-containing $Fe^{(II)}$ complex (Scheme 3d) undergoes C–hydroxyl bond breakage to generate the CO-bound $Fe^{(II)}$ species (Scheme 3e). A comparable process has been proposed for the electrochemical reduction of CO_2 using iron porphyrins. In this pathway, the Fe–COOH intermediate is thought to undergo a concerted proton–electron transfer bond cleavage (CPETBC). This step involves proton transfer from a donor in the reaction medium, simultaneous electron transfer from the metal center, and cleavage of one of the C–O bonds. This CPETBC step is believed to be the rate-limiting stage in the overall homogeneous CO_2 electroreduction process (Scheme 3d to e′).[50]

In the FeTEsCCl iron chlorin complex which contains a secondary H^+ transfer site (Scheme 4A(a)), CO_2 reduction and activation proceed from the $Fe^{(I)}$ oxidation state (Scheme 4A(c)), while the $Fe^{(0)}$ state is typically responsible for reactivity in iron porphyrin systems. Simultaneous binding of CO_2 and a proton to $Fe^{(I)}$TEsCl leads to the formation of the COOH-containing $Fe^{(III)}$ intermediate (Int-I; Scheme 4A(d)). Mössbauer spectroscopy reveals that this species has $\Delta E\_q = 0.68$ mm s^{-1} and $\delta_{iso} = 0.31$ mm s^{-1}, closely matching the values for the initial $Fe^{(III)}$–Cl complex ($\Delta E\_q = 0.67$ mm s^{-1}, $\delta_{iso} = 0.30$ mm s^{-1}), which is consistent with a high-spin ferric state ($S = 5/2$). Vibrational spectroscopy identifies C═O and Fe–C stretching bands at 1724 cm^{-1} and 561 cm^{-1}, respectively, with ^{13}C labeling confirming these assignments. This COOH-containing $Fe^{(III)}$ intermediate is reduced by one electron either through chemical means or electrochemically at $E_0 = -0.64$ V *vs.* $Fc^{+/0}$ to produce the COOH-containing $Fe^{(II)}$ species (Int-II; Scheme 4A(e)). Mössbauer spectroscopy of the reduced complex shows $\Delta E\_q = 2.41$ mm s^{-1} and $\delta\_iso = 0.81$ mm s^{-1}, which is consistent with a high-spin $Fe^{(II)}$ ground state ($S = 2$). The C═O stretching frequency shifts to 1682 cm^{-1}, which is lower than the 1724 cm^{-1} observed for the COOH-containing $Fe^{(III)}$ species. This suggests that the $Fe^{(II)}$ center donates more electron density into the CO π* orbital. The $Fe^{(II)}$ species containing

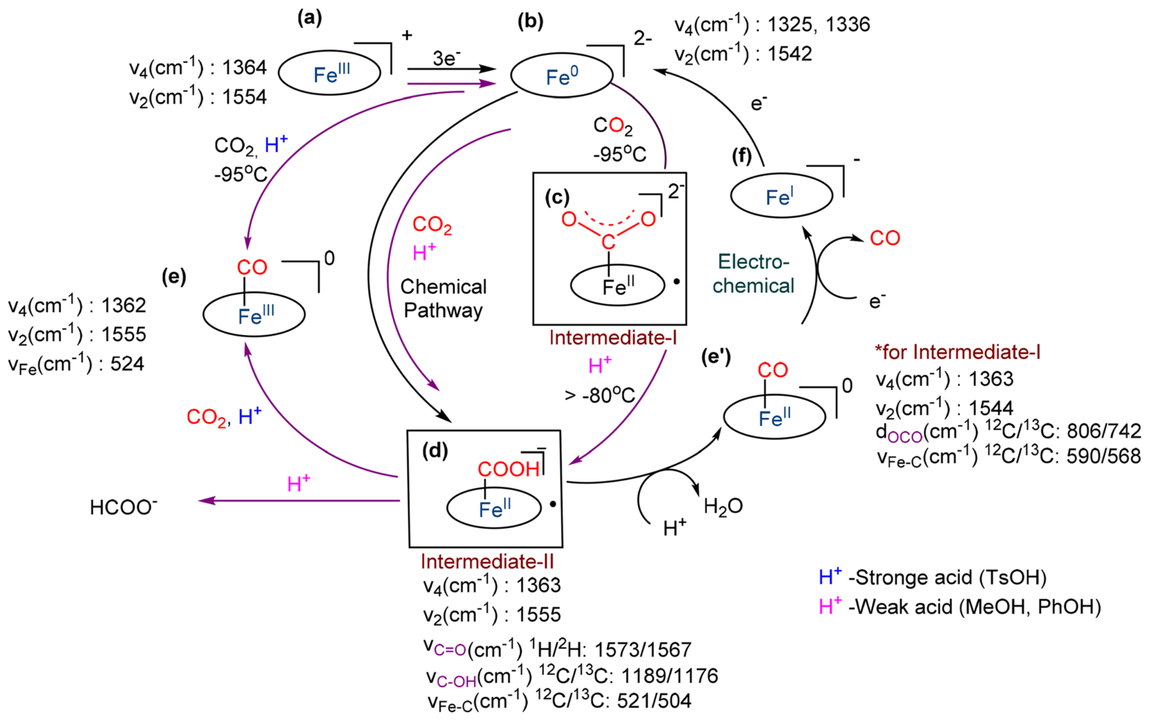

Scheme 3 Mechanistic pathway for CO_2 reduction using the Fe-catalyzed porphyrins.

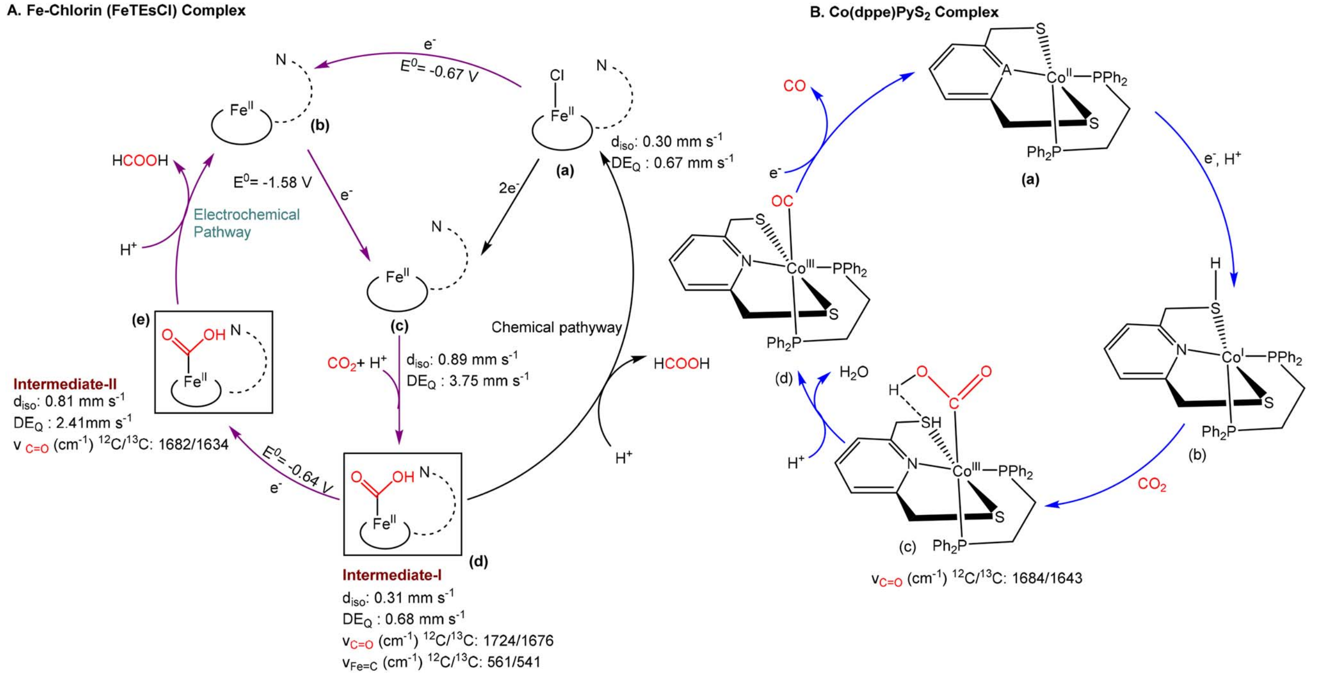

Scheme 4 Suggested catalytic pathway for CO_2 reduction.

a COOH group is also detected during *in situ* FTIR spectroelectrochemical experiments, suggesting that its decomposition represents the rate-determining step in the catalytic cycle (Scheme 4A(e)). Ultimately, cleavage of the Fe–C bond leads to the formation of formic acid[53] in the Co(dppe)PyS$_2$ species, which was modeled after the active part of the enzymes (Ni–CODH) (Scheme 4B(a)). The reduction of CO_2 is initiated with the protonation of the metal-bound thiolate, which occurs alongside the reduction of the cobalt center from $Co^{(II)}$ to $Co^{(I)}$ (Scheme 4B, step a to b). CO_2 then binds to the reduced $Co^{(I)}$ center, forming a COOH-containing $Co^{(III)}$ species (Scheme 4B(c)). This species shows a C═O stretching frequency at 1684 cm^{-1} which shifts to 1643 cm^{-1} when $^{13}CO_2$ is used, confirming the identity of the CO_2-derived ligand. DFT calculations support this assignment and indicate that the electronic configuration corresponds to a low-spin ($S = 0$) COOH-containing $Co^{(III)}$ intermediate. This intermediate eventually undergoes cleavage of the COH bond, releasing CO as the final product (Scheme 4B(d)).

2.2. Effect of hydrogen bonding

Recently, it has been investigated how internal and external Brønsted acids with varying pK_a values influence catalytic performance. Interestingly, the most effective catalysts contained internal groups with relatively weak acidity. Overall, the optimization of CO_2 reduction by porphyrin-based catalysts involves careful consideration of solvent hydrogen bonding, the spatial arrangement of internal H-bond donors, and the interplay between the pK_a values of both internal and external acid sources.[98–101] Iron porphyrin complexes, including FePf (A), FeTDHPP (B), FeEs$_4$ (C), and Fe(^{t}Bu)$_4$ (D), were studied to investigate how second-sphere donors influence the kinetics of CO_2 reduction and hydrogen bonding. These complexes varied in the design of their distal framework or outer coordination environment. In FePf, the amide group serves as a relatively weak hydrogen bond donor (CON–H pK_a = 22 in CH_3CN) compared to the phenolic OH group in FeTDHPP, which has a higher pK_a of 29.14 in CH_3CN, indicating stronger hydrogen bonding ability. The large pivaloyl group in FePf creates a hydrophobic setting around the active site. On the other hand, FeEs$_4$ features a hydrophilic environment near the catalytic center, resulting from the presence of four triazole units that help retain water molecules. The Fe(^{t}Bu)$_4$ complex exhibits an amphiphilic local environment, characterized by hydrophilic triazole groups adjacent to the active site and a hydrophobic periphery formed by the *tert*-butyl ligands (Fig. 4).

Dey and coworkers performed a systematic study of the influence of electrostatic interactions and hydrogen-bonding substituents at the *ortho* position of the mesophenyl groups in an iron tetraphenylporphyrin, revealing that both play a significant role in enhancing the reduction selectivity of CO_2. The effect of hydrogen bonding becomes stronger with increasing water concentration as water facilitates these interactions. In contrast, the impact of electrostatic interactions diminishes at higher water levels because solvation of the cationic groups alters the microsolvation environment around the active site, promoting proton reduction to H_2 over CO_2 reduction. These findings emphasize an important distinction between electrostatic interactions and hydrogen-bonding in controlling electrochemical CO_2 reduction selectivity depending on water content, highlighting the need to consider such factors when designing practical CO_2 reduction systems that use water as a sustainable proton source.[102] Using phenol as the

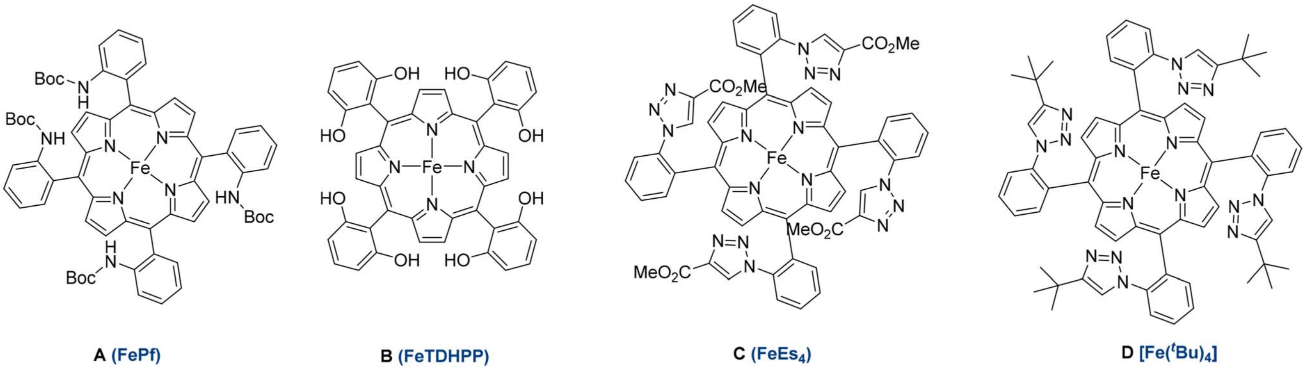

A (FePf) **B (FeTDHPP)** **C (FeEs$_4$)** **D [Fe(^{t}Bu)$_4$]**

Fig. 4 Iron porphyrin complexes examined to evaluate the second-sphere interactions.

external H^+ donor, the FePf demonstrated the fastest reaction rate attributed to the stabilization of the intermediate $Fe^{(II)}$–COO^{2-} by favorably aligned amide dipoles. Across these complexes, a fourfold dependence on the PhOH concentration was observed, and a clear relationship was established between the CO_2 reduction rates and the pK_a values of the H-bonding groups in various iron porphyrin systems; however, it might seem intuitive to attribute the improved CO_2 reduction rates mainly to hydrogen-bonding stabilization (Fig. 5).[103]

The observed correlation was supported by DFT calculations, which suggested that electrostatic effects also play a key role by stabilizing the electron density transfer to the coordinated CO_2 during activation. This conclusion aligns with previous findings from the Savéant, Nippe, Aukauloo and Mayer groups, all of which reported increased catalytic activity upon incorporating cationic groups near the catalytic center (Fig. 6).[68–71,104] In summary, amine, pyridine, imidazole, guanidine, phenol, amide, urea, thiourea, ester and ether groups have been utilized as the hydrogen-bond donor in the second coordination sphere of Fe, Re, Mn, Co and other transition-metal-based complexes. The hydrogen-bond interaction can assist catalyst molecules in adsorbing CO_2 and stabilizing the intermediates of the CO_2 reduction, thereby improving the catalytic activity and product selectivity of electrocatalytic CO_2RR. By adjusting the positioning accuracy and strength of the hydrogen-bond interaction through appropriate structural modification in the second coordination sphere, transition-metal complexes show anticipated potential for homogeneous electrocatalytic CO_2 reduction (Scheme 5).[98] Furthermore, hydrogen-bond interaction and proton concentration may work together to regulate the reduction pathway, so they change the selectivity and catalytic activity of the product. For instance, the intermediate M–COOH is usually formed during the CO_2 reduction reaction and the protonation on the M–COOH could affect the type of reduction products. CO is formed after the protonation of the O-center, whereas HCOOH is released after the protonation of the C-center. The protonation process can be determined by the pK_a values of the C or O centers and the hydrogen-bond interaction, which also provides a new idea for regulating the types of CO_2 reduction products.[105–107]

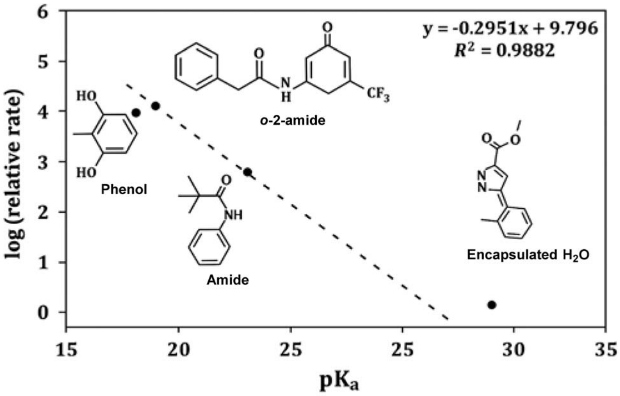

Fig. 5 Relative rate *vs.* pK_a.

2.3. Divergence point between CO and HCOOH formation

Spectroscopic evidence provides a basis for developing a molecular orbital diagram of the metal–COOH complex. The carboxylate HOMO originates from an sp^2 carbon and can form σ-type bonds with the metal d_{z^2} orbital. Meanwhile, the carboxylate unoccupied LUMO is a C–O π* orbital capable of accepting electron density from the metal-filled d_{xz} and d_{yz} orbitals *via* π back-donation (Fig. 7). The subsequent reactivity of this metal–carboxylate intermediate plays a crucial role in determining the selectivity of the two-electron, two-proton CO_2 reduction, directing the pathway toward either formic acid or carbon monoxide production. Protonation at the oxygen atom leads to CO release along with water elimination, whereas protonation at the carbon atom yields HCOOH. This selectivity can be influenced by tuning the pK_a values of the oxygen or carbon centers, which are governed by the nature of their bonding interactions. A strong C–Fe σ bond withdraws electron density from the carbon atom, thereby increasing the protonation susceptibility of the oxygen atom and facilitating C–O bond cleavage, which leads to CO formation. In contrast, a weaker C–Fe σ bond results in greater electron density on the carbon, favoring protonation at the carbon site and promoting the formation of formic acid. Additionally, significant dπ to C=O π* back-donation enhances electron density in the π* orbital, primarily located on the oxygen atom, making it more

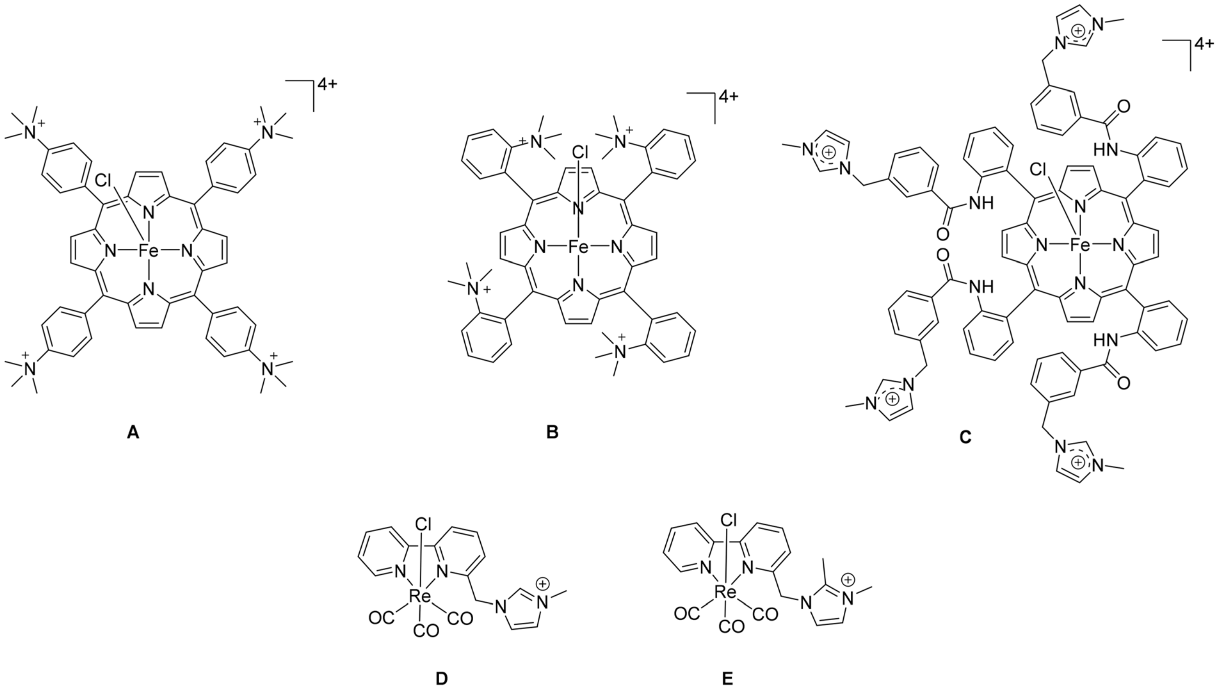

Fig. 6 Catalysts showing improved reaction rates when cationic groups are incorporated into the ligand framework.

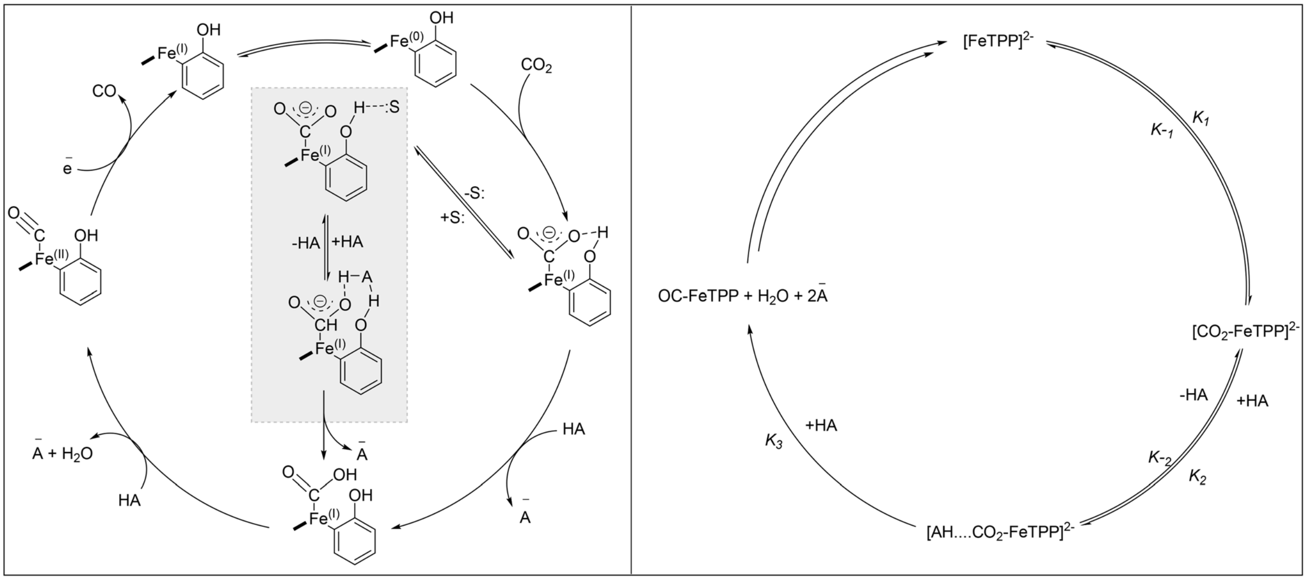

Scheme 5 Iron porphyrin-mediated CO_2 reduction mechanism assisted by H-bonding.

prone to protonation and further encouraging cleavage of the C–O bond. However, C–M σ bonding typically plays a more dominant role in defining the C–M interaction, as evidenced by observations in Fe–O_2 complexes.[70] In the context of CO_2 reduction, the bonding interactions within the M–COOH intermediate are notably influenced by the effective nuclear charge (Z_{eff}), which itself is governed by the metal center spin state (Δ°). Low-spin configurations typically result in a greater population of dπ orbitals, enhancing π back-donation to the C═O π* orbital. This increases the electron density on the oxygen atom, promoting protonation at the O-site and favoring C–O bond cleavage, ultimately leading to CO formation. Conversely, high-spin states which limit π back-donation tend to favor protonation at the carbon center, resulting in HCOOH production. These insights underscore the critical role of the spin state in dictating the product selectivity of the CO_2 reduction pathway.

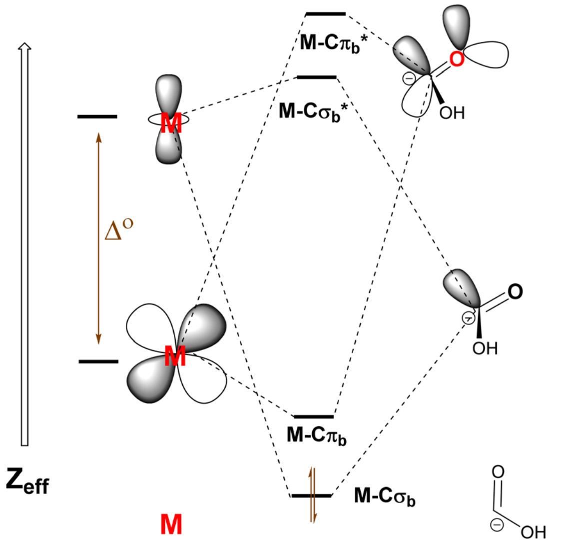

Fig. 7 Illustrative MO diagram of the M–COOH species depicting principal bonding interactions.

For the COOH-containing Co$^{(III)}$ intermediate formed by the Co(dppe)PyS$_2$ complex, the low-spin t$_2$^{6} electronic configuration leads to a highly covalent Co$^{(III)}$–carbon bond. DFT studies also suggested that this strong covalent interaction effectively withdraws charge density from the carbon atom. As a result, the electron-deficient carbon enhances the electrophilicity of the oxygen site that favors its protonation. This pathway facilitates C–O bond cleavage and ultimately promotes the selective release of CO.[108] The impact of the spin state on the product selectivity is evident when comparing the COOH-bound Fe$^{(II)}$ intermediates in iron chlorin and iron porphyrin complexes. For iron porphyrins such as FeEs$_4$, resonance Raman studies confirm a low-spin Fe$^{(II)}$ ground state, which aligns with the selective two-electron, two-proton electrochemical reduction of CO$_2$ to CO involving C–O bond cleavage through oxygen protonation. Conversely, the COOH-bound Fe$^{(II)}$ intermediate from the iron chlorin complex (Fig. 3e) exhibits a high-spin configuration and exclusively produces HCOOH. While the presence of hydrogen-bonding groups or second-sphere proton-transfer influences the outcome, the spin state also plays a pivotal role when considered through the lens of molecular orbital theory. The low-spin metal carboxylic intermediates favor CO release, whereas the high-spin carboxylic intermediates species promote HCOOH formation.

The recent finding that iron tetraphenylporphyrin produces HCOOH and not CO from CO$_2$ when an amine ligand binds opposite the CO$_2$ might be due to a change in spin state caused by the strong σ-donor ligand binding.[109] A distinctive pentadentate azamacrocyclic ligand framework exhibits a shift in product selectivity from CO to HCOOH when the metal center is changed from cobalt(II) to iron(III).[110] CO$_2$ coordination to a formal Co$^{(0)}$ complex results in the formation of a putative COOH-bound Co$^{(II)}$ intermediate. Conversely, when CO$_2$ interacts with a formal Fe$^{(I)}$ species, it gives rise to a proposed COOH-bound Fe(III) intermediate. In the case of cobalt, strong π back-donation from the Co$^{(II)}$ center into the π* orbitals of CO$_2$ is believed to weaken the C–O bond, thereby favoring the generation of CO. On the other hand, weaker π back-bonding from the Fe$^{(III)}$ center keeps the C–O bond strong and results in a low charge density on the oxygen atom. The Lou team performed kinetic and product determinations of the reaction of the simplest Criegee intermediate CH$_2$OO with HCHO by employing the highly flexible mid-infrared comb lasers and synchronized two-color time-resolved dual-comb spectroscopy. The bimolecular rate coefficients for the reaction CH$_2$OO + HCHO were evaluated over the temperature range of 268.6 to 336.5 K at a total pressure of 6.4 to 56.0 torr.[111] Alternatively, the introduction of strategically positioned H$^+$ transfer sites has been demonstrated to enhance the selective reduction of CO$_2$ to CO in iron porphyrins, cobalt azacalix-pyridyl systems and metal bipyridine complexes (Fig. 3 and 4).[64,103,112–114] While the exact role of spin state in determining selectivity in these systems still needs further investigation, it is probable that the strong equatorial ligand fields in porphyrin and azacalix-pyridyl complexes stabilize low-spin metal–COOH intermediates, leading to the selective formation of CO. In summary, factors such as spin state, back-bonding and the surrounding second-sphere environment can influence the pK_a values of the carbon and oxygen atoms in metal–COOH intermediates. Further investigation is required to identify which factors predominantly influence the structure of these intermediates and ultimately govern the selectivity of the two-electron, two-proton CO$_2$ reduction process. The key reaction intermediates for CO$_2$ conversion to CO and HCOOH are *COOH and *OCHO, respectively, although the adsorption structure (*e.g.*, monodentate, bidentate) has not been definitively determined. Furthermore, the competition between the CO and HCOOH pathways has generally been attributed to differences in the reaction energy barriers for forming *COOH and *OCHO, with some studies suggesting that *H adsorption also plays a significant role. Beyond thermodynamic factors, recent research indicates that reaction kinetics are crucial in influencing product distribution. Moreover, an accurate description of the CO$_2$RR mechanism requires consideration not only of internal factors (*e.g.*, binding energy, reorganization energy), but also external factors (*e.g.*, pH, applied potential, and metal cations in the electrolyte). These mechanistic insights and recent studies on catalysts with tunable selectivity toward CO and HCOOH demonstrate how variations in the structure, oxidation state, composition, and coordination environment can direct a metal's selectivity between these two products.[115–117]

2.4. Divergence between CO$_2$ reduction and hydrogen evolution

Metal centers capable of binding and reducing CO$_2$ are typically electron-rich, which often results in proton reduction competing with the CO$_2$RR. When protonation occurs at an metal center, it generates an M^{n+2}–H intermediate that can react either with CO$_2$ or with protons (Scheme 6). The reaction with protons may proceed more readily, favoring hydrogen evolution as the primary outcome. In contrast, insertion of CO$_2$ into the

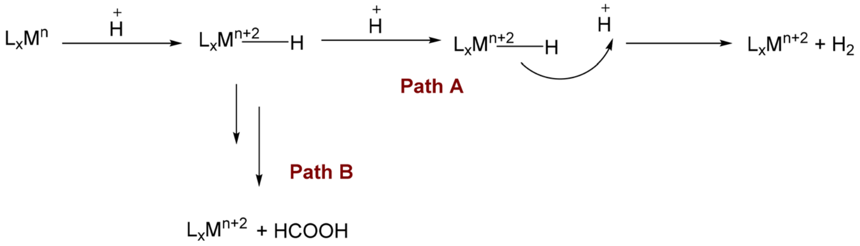

Scheme 6 Competing reactivity: CO_2 *vs.* proton reduction.

metal–hydride bond (pathway B) leads selectively to the formation of formic acid.[118,119] The hydricity of the metal–hydride species is a key factor influencing both the thermodynamic and kinetic aspects of this competing process.[120,121] The challenge of competing the HER can be addressed by strategies that enhance CO_2 coordination at the metal center, while steering protonation toward the ligand, thus avoiding protonation at the metal itself. This approach involves adjusting the metal electronic properties to lower its basicity and incorporating an electron-rich ligand framework. For example, in Ni–cyclam and Fe–chlorin complexes, CO_2 binds to the metal center in a formal +1 oxidation state rather than the zero-oxidation state. This oxidation state preference reduces the tendency for protonation at the metal, and thus lowers the chance of competing hydrogen evolution reaction.[78,122] A Ni-CODH-inspired ligand featuring an electron-rich thiolate group can act as a preferred site for protonation, thereby inhibiting protonation at the metal center and enabling effective CO_2 coordination. This strategy has recently been demonstrated in two cobalt complexes (Fig. 3f).[108,123] A positive shift in the metal center's reduction potential reduces the reaction overpotential. Additionally, these protonated moieties enhance the stability of the Mn^{2+}–CO_2^{2-} intermediate by facilitating proton transfer, leading to the formation of the Mn^{2+}–CO_2H species.[124]

Another strategy utilizes the reductive disproportionation of CO_2 into CO and CO_3^{2-}, eliminating the need for a H^+ source and enabling selective CO production. This strategy has been successfully applied in various metal phosphine complexes, as well as in manganese–bipyridine systems (Fig. 3g).[64,66,93,125] Moreover, in their earlier studies, the Yang group focused on how the hydricity of transition metal hydrides varies with solvent and how this influences the thermodynamics of CO_2 reduction to formate (HCO^{2-}). They also demonstrated how hydricity values can inform the design of catalysts for both the HER and CO_2 reduction (CO_2R), establishing a general framework for achieving selective formate production while minimizing undesired H_2 formation. By analyzing kinetic data from proposed catalytic cycles, they identified potential rate-limiting steps in both the HER and CO_2R pathways. To enhance the selectivity for CO_2 reduction, the group also pursued two catalyst design strategies aimed at kinetically suppressing HER: one leveraging electrostatic interaction through charged environments, and the other employing steric hindrance. These strategies, alongside thermodynamic considerations such as hydricity and the free energy profiles of catalytic steps, guided the development of electrocatalysts capable of reversible CO_2/formate conversion at low overpotentials. Furthermore, they explored the translation of CO_2 hydrogenation activity from homogeneous catalysis into the realm of electrocatalysis. All of the studied systems utilized classical metal hydrides, where both the electrons and proton reside on the metal center. However, generating hydrides strong enough for CO_2 reduction typically demands highly reducing potentials due to the intrinsic link between the reduction potential, hydricity, and pK_a. In contrast, the enzyme formate dehydrogenase (FDH) demonstrates a different mode of hydride delivery—bidirectional transfer, in which the proton and electrons are spatially separated. This bioinspired mechanism offers a compelling strategy for producing potent hydride donors under milder electrochemical conditions. It presents a new direction for catalyst design, suggesting that hydricity can serve as a powerful tool in addressing longstanding challenges and unlocking new possibilities in catalytic CO_2 conversion.[126–130]

3. Photocatalytic CO_2RR

Photocatalytic CO_2 reduction methods are grouped as either heterogeneous or homogeneous processes. Heterogeneous approaches predominantly utilize solid photocatalysts like semiconductors or plasmonic metals. As depicted (Fig. 8a), the semiconductor-driven photocatalytic CO_2 reduction mechanism comprises at least three essential steps.[124,131] Initially, absorption of light with photon energy matching or surpassing the semiconductor's bandgap excites electrons from the valence band maximum (VBM) to the conduction band minimum (CBM), generating holes at the VBM. Subsequently, these photogenerated charge carriers migrate to the catalyst surface, potentially mediated by a cocatalyst. Finally, adsorbed CO_2 undergoes reduction through interaction with the electrons, while adsorbed reductant molecules are oxidized by the holes. Ideally, CO_2 reduction occurs simultaneously with water oxidation or other beneficial oxidation reactions. Crucially, this process must meet two thermodynamic criteria: the reduction half-reaction's redox potential must be less negative (more positive) than the CBM potential, and the oxidation half-reaction's redox potential must be less positive (more negative) than the VBM potential. Scheme 1 lists common CO_2 reduction half-reactions and their apparent standard redox potentials at pH 7. Additionally, effective reaction kinetics necessitate the presence of catalytic sites capable of activating CO_2 molecules.

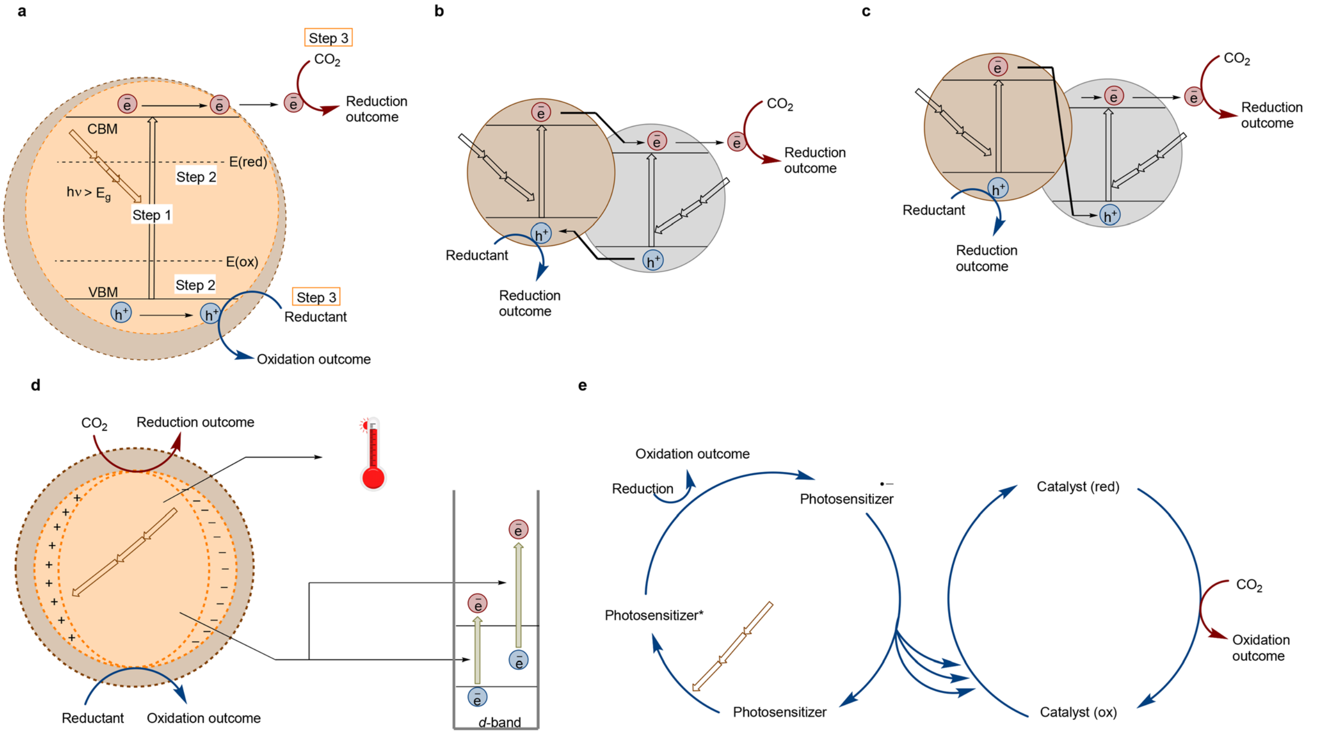

Fig. 8 Principles of photocatalytic CO_2 reduction.

Fabricating heterostructure catalysts that feature favorable band alignment is an effective strategy to achieve a broad spectral response and efficient charge separation.

Such catalysts are subdivided into p–n junction and Z-scheme configurations, according to their charge transfer pathways.[132–136] Within a p–n junction heterostructure (Fig. 8b), photo-generated electrons transfer to the component possessing the more positive conduction band (CB) potential, while photo-generated holes migrate toward the component with the more negative valence band (VB) potential. In contrast, Z-scheme architectures (Fig. 8c) operate differently: electrons photo-generated in the component having the more positive CB potential transfer directly into the valence band of a second component with a more negative VB potential, or indirectly *via* conductive mediators or reversible redox shuttles. Furthermore, metals like gold, silver, copper, and bismuth can facilitate heterogeneous photocatalytic CO_2 reduction, an activity largely attributed to their localized surface plasmon resonance (Fig. 8d).[137–140] Specifically, incident photons at the resonant frequency excite collective electron oscillations. This subsequently produces local heat and generates hot carriers *via* intraband (s-to-s) or interband (d-to-s) transitions under intense surface electric fields. Both the localized thermal energy and these hot carriers can drive CO_2 reduction.[141–143] The fundamental steps in homogeneous photocatalytic CO_2 reduction mirror those of semiconductor-based systems, but differ in employing a photosensitizer and molecular catalyst. As illustrated (Fig. 8e), light absorption first excites the photosensitizer, which is subsequently reductively quenched by a sacrificial electron donor, yielding its reduced form.[143]

This reduced species then transfers electrons to the molecular catalyst, converting it from an oxidized to reduced state. Subsequently, the reduced catalyst donates electrons to CO_2, driving its reduction. The alternative oxidative quenching pathway is less prevalent in CO_2 reduction systems.[144] Hybrid approaches also exist where molecular catalysts anchor to semiconductor surfaces *via* covalent or non-covalent bonds.[145] In these configurations, the semiconductor generates charge carriers upon illumination, while the tethered molecular catalyst functions as a cocatalyst, providing specialized sites for CO_2 activation and reduction.

3.1. Site-isolating molecular catalysts by TiO_2 heterogenization

Although the tricarbonyl Re(I) complex, (bpy)$Re^I(CO)_3Cl$, recognized for its near-perfect selectivity in catalyzing CO_2 reduction to CO (>99%), alternative dimeric catalytic routes have also been observed to yield CO, along with the partial conversion of CO_2 into bicarbonate (HCO_3^-).[2,146–152] The formation of various binuclear intermediates during the catalytic process indicates that the reduced $Re^{(I)}$ species undergo notable mutual interactions throughout the reaction (Scheme 7). Under these uncontrolled conditions, undesirable side reactions often take place in conventional Re(I)-based catalysis, leading to structural degradation of the original catalyst and causing premature loss of catalytic activity.

Chemical fixation of the $Re^{(I)}$ catalyst onto a TiO_2 semiconductor was found to induce site isolation. This promotes

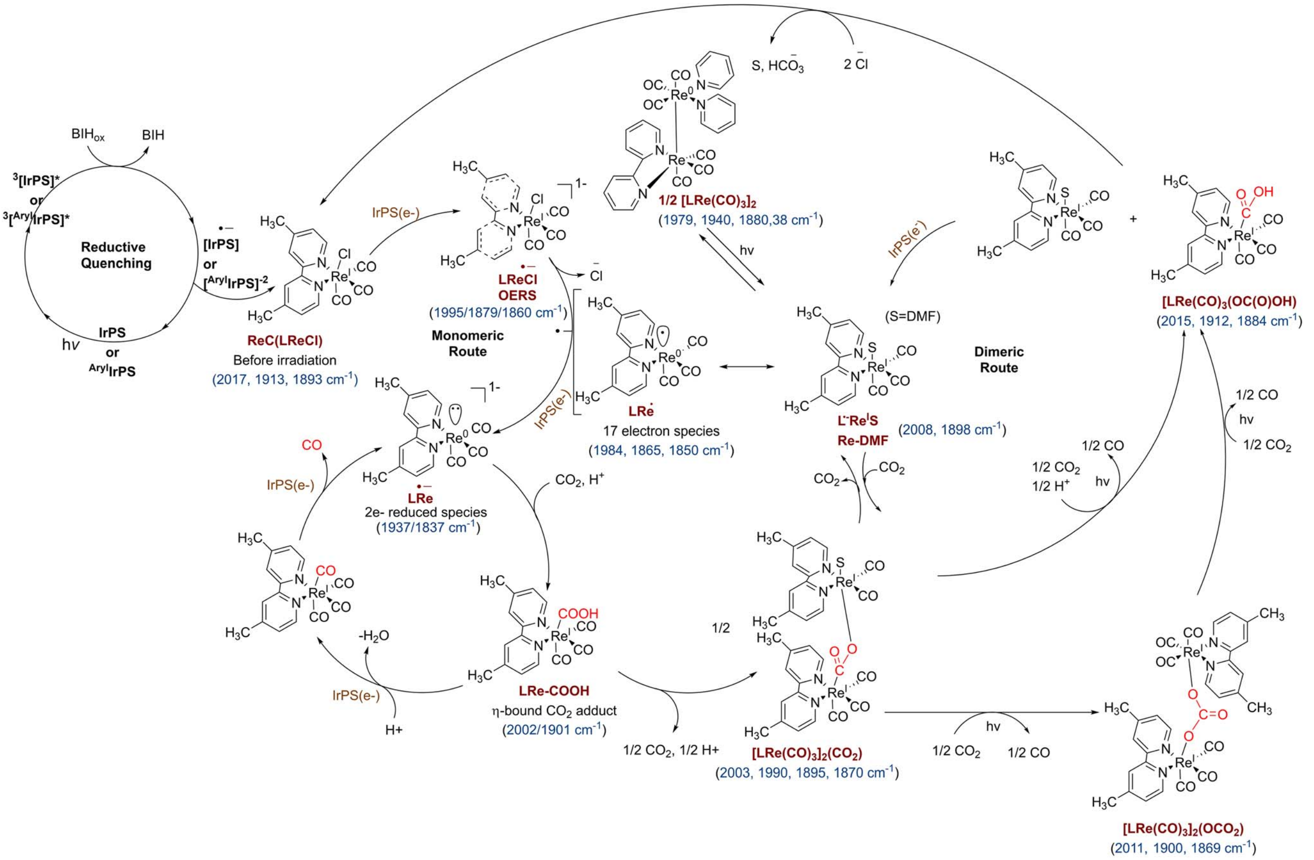

Scheme 7 Schematic of the monomeric and dimeric photochemical CO_2 reductions.

operation *via* the monomeric catalytic pathway, resulting in improved activity and durability (Scheme 8).[152]

An *operando* FTIR spectrophotochemical comparison between the free $Re^{(I)}$ catalyst and its TiO_2-anchored counterpart confirmed that TiO_2 immobilization significantly suppresses the formation of Re–Re dimeric intermediates, a key pathway associated with catalyst deactivation. Additionally, the *fac*-[(4,4′-Y_2-bpy)$Mn^I(CO)_3Br$] catalyst (MnP, Y = $CH_2PO(OH)_2$) was appended to the dye-sensitized TiO_2 platform employed for photochemical CO_2 reduction. The efficient visible-light sensitization of this platform allows the TiO_2 particles to function effectively as an electron supplier.[153] The Mn(I)-based hybrid system (dye/TiO_2/MnP) demonstrated sustained photocatalytic performance, achieving high turnover numbers (TONs), along with outstanding selectivity for formate production over CO (Scheme 9). *In situ* FTIR spectrophotochemical analysis revealed that the catalytic mechanism (involving monomeric Mn–H or dimeric Mn–Mn intermediates) depends on $Mn^{(I)}$ surface loading. Low Mn concentrations favor the monomeric Mn–H pathway producing formate ($HCOO^-$), while high concentrations promote the dimeric Mn–Mn mechanism yielding CO. Specifically, under visible light with 0.1 M electron donor and 0.001 M $LiClO_4$, a hybrid catalyst with low MnP loading (0.1 μmol per 10 mg TiO_2) generated formate exclusively (>99% selectivity) with a turnover number (TON) of ∼250 after 23 hours of irradiation.[153]

These findings highlight that anchoring the molecular $Mn^{(I)}$ catalyst onto the TiO_2 surface provides effective spatial separation, which minimizes the formation of dimeric intermediates and curbs side reactions arising from interactions between reactive Mn species. This spatial isolation significantly improves both the catalytic activity and product selectivity of the MnP-heterogenized MIOM system. Expanding this approach to a monobipyridyl $Ru^{(II)}$ catalyst revealed distinct behavior. Unlike the highly selective CO/formate production typical of bipyridyl $Re^{(I)}$ or $Mn^{(I)}$ systems, the homogeneous (bpy) $Ru^{II}(CO)_2X_2$ complex (bpy = modified 2,2′-bipyridine; X = halide) mediates CO_2 reduction through an inherently more complex mechanism. Significant $Ru^{(I)}$ dimerization occurs under catalytic conditions.[125,143,144,154–157] Naturally, the tendency of Ru–Ru dimerization promotes significant self-polymerization, forming polymeric $Ru^{(II)}$ chains ($-(L(CO)_2Ru-Ru(CO)_2L)_n-$) which ultimately precipitate out as an inactive complex, causing premature loss of catalytic activity.[158,159]

TiO_2 immobilization offers a viable strategy to improve the catalytic efficiency and durability of the bipyridyl Ru(II) complex, as shown by these results.[160] Sequential *operando* FTIR and photophysical studies revealed that anchoring the molecular $Ru^{(II)}$ catalyst, (4,4′-Y_2-bpy)$Ru^{II}(CO)_2Cl_2$ (RuP) (Y = $CH_2PO(OH)_2$), onto a TiO_2 semiconductor effectively stabilizes the key monomeric intermediate, (bpy)Ru(H)$(CO)_2$Cl (Ru–H). This heterogenization also significantly suppresses the formation of

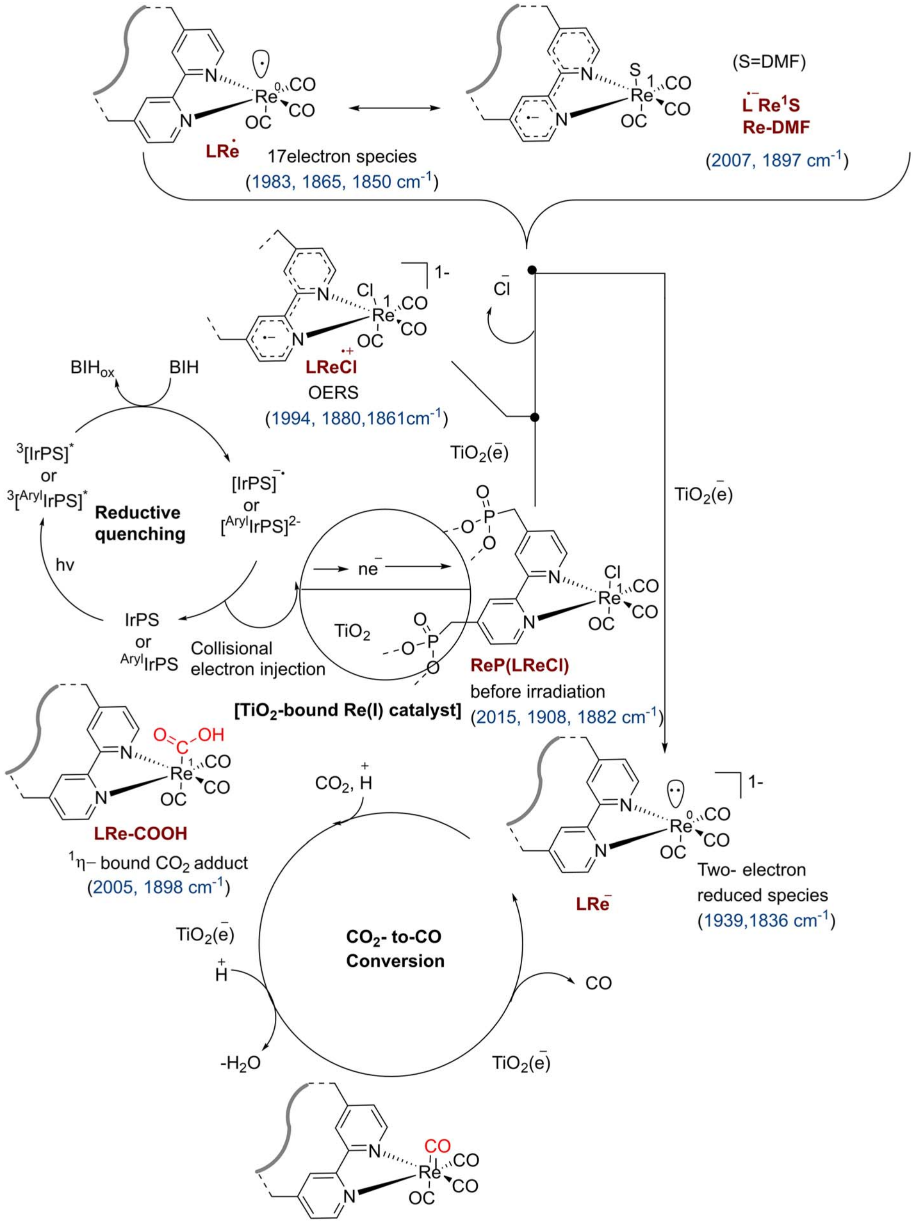

Scheme 8 Mechanistic pathways of the supported $Re^{(I)}$ catalyst in photochemical CO_2 reduction by the mixed heterogeneous binary system.

the polymeric $Ru^{(II)}$ species, a major degradation pathway observed in homogeneous photolysis with the molecular $Ru^{(II)}$ catalyst. Consequently, selective promotion of the monomeric $Ru^{(II)}$ pathway on TiO_2 significantly enhanced both photocatalytic activity and durability relative to the homogeneous IrPS + Ru(II) system. Under optimal conditions, the semi-heterogeneous IrPS + TiO_2/RuP strategy achieved maximum TONs exceeding 4816 (CO) and 2228 (formate) after 22 h of photolysis.

3.2. Tuning MIOM architectures for cooperative catalytic performance

The TiO_2 semiconductor serves as an effective scaffold for multifunctional hybrid systems, where multiple molecular catalysts operate simultaneously within a single MIOM platform. For instance, syngas (H_2 + CO) a key feedstock for Fischer–Tropsch synthesis can be photochemically coproduced in a tunable manner using a dual-function MIOM system (dye/TiO_2/ReP:CoP). This system integrates the co-immobilized hydrogen evolution catalyst $[Co^{III}Cl(dimethylglyoximato)_2(pyridyl\text{-}4\text{-}phosphonic\ acid)]^-$ (CoP) and the CO_2-to-CO reduction catalyst *fac*-[Re^I(4,4′-bis(dihydroxyphosphorylmethyl)-2,2′-bipyridine)$(CO)_3$Cl] (ReP) on TiO_2 particles (Scheme 10). Photolysis experiments demonstrated tunable syngas H_2 : CO ratios from 1 : 2 to 15 : 1 by adjusting the water content and ReP/CoP surface loadings. This offers a strategic framework for designing photochemical syngas systems with controlled H_2/CO composition.[161] This finding offers valuable insight for guiding the design and development of next-generation photochemical syngas production systems capable of precisely controlling the H_2/CO ratio.

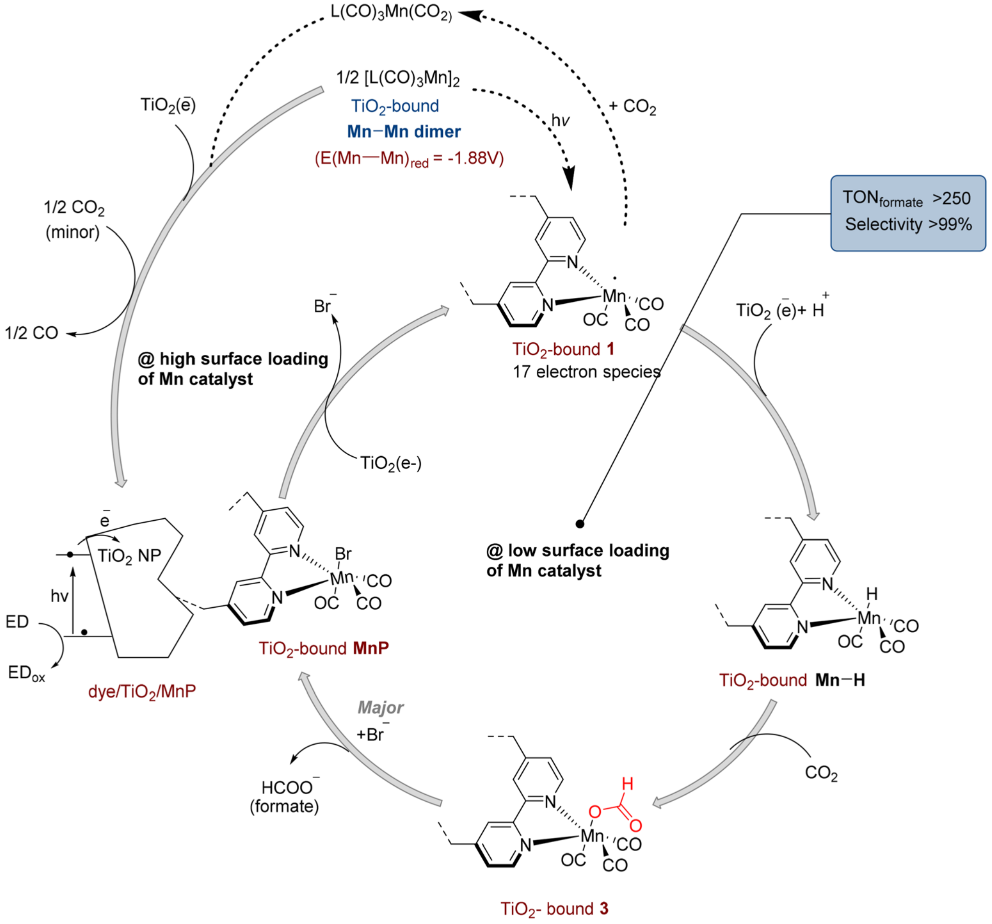

Scheme 9 Proposed MnP-concentration- and intermediate-dependent mechanistic pathways in photochemical CO_2 reduction by the ternary hybrid system.

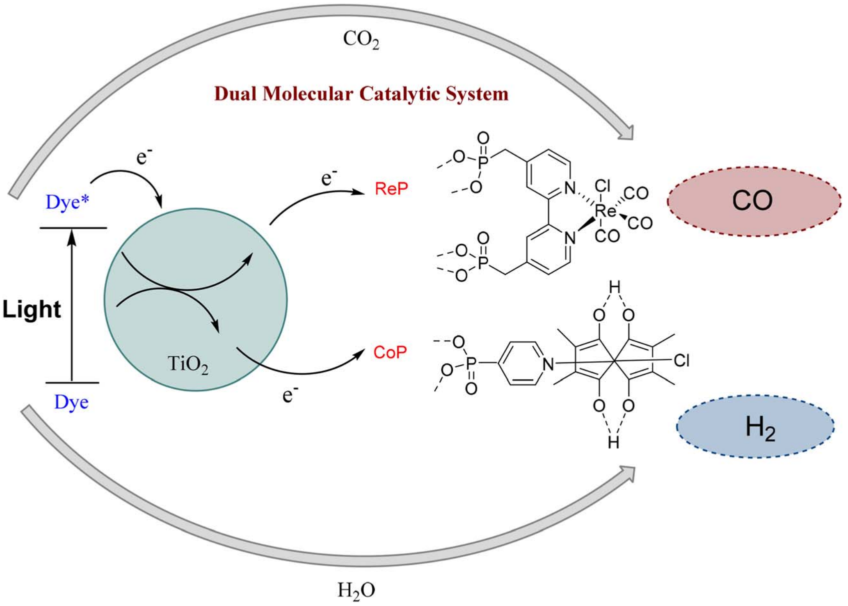

Scheme 10 Multifunctional hybrid assembly: dye–TiO_2–ReP:CoP.

3.3. Mechanistic and electronic control of catalysts *via* TiO_2 heterogenization

Importantly, the n-type TiO_2 semiconductor modulates the electronic structure of chemisorbed metal complexes. The catalytic CO_2 reduction efficiencies of homogeneous $[Cp^*Ir^{III}(4,4'\text{-}Y_2\text{-bpy})Cl]^+$ (Y = $CH_2PO(OEt)_2$; Cp*IrPE) and TiO_2-immobilized $[Cp^*Ir^{III}(4,4'\text{-}Y_2\text{-bpy})Cl]^+$ (Y = $CH_2PO(OH)_2$; Cp*IrP) catalysts in IrPS-sensitized MIOM systems (homogeneous: IrPS + CpIrPE; heterogeneous: IrPS/TiO_2/CpIrP) (Scheme 11).[162] The IrPS/TiO_2/CpIrP hybrid produces comparable quantities of formate and CO during photolysis, revealing that the TiO_2-immobilized CpIrP catalyst facilitates both CO_2-to-formate and CO_2-to-CO conversions. This contrasts with homogeneous solvated Cp*IrPE, which exclusively generates formate. Mechanistic studies combining photophysical and electrochemical analyses indicate that the electron-withdrawing effect of the TiO_2 support lowers the hydricity of the $Ir^{(III)}$ hydride intermediate, promoting its deprotonation in the presence of the base additive TEOA. This conversion of $[Cp^*(bpy)Ir^{(III)}\text{–}H]^+$ and TEOA to $[Cp^*(bpy)Ir(I)]^0$ and $TEOAH^+$ enables CO_2 reduction to CO through the formation of the η^1-bound $[Cp^*(bpy)Ir^{(III)}(C(O)OH)]^+$ intermediate. In contrast, systems lacking TiO_2 anchoring mainly favor formate production. This mechanistic pathway is supported by both the observed TEOA-dependence of CO formation and UV-vis absorption data, which reveal a notable red shift (approximately 30 nm) in the MLCT (metal-to-ligand charge transfer) bands specifically from $Ir^{(III)}$ d-orbitals to the bipyridine ligand when Cp*IrP is immobilized on n-type TiO_2 compared to its behavior on ZrO_2 or in DMF solution.

4. Single atom alloys for CO_2RR

Single-atom alloying (SAA) represents a powerful strategy to enhance the catalytic performance of metals in CO_2 reduction. By anchoring isolated metal atoms onto the surface of a host metal, SAA catalysts integrate the distinctive characteristics of both components, while preserving the advantages inherent to

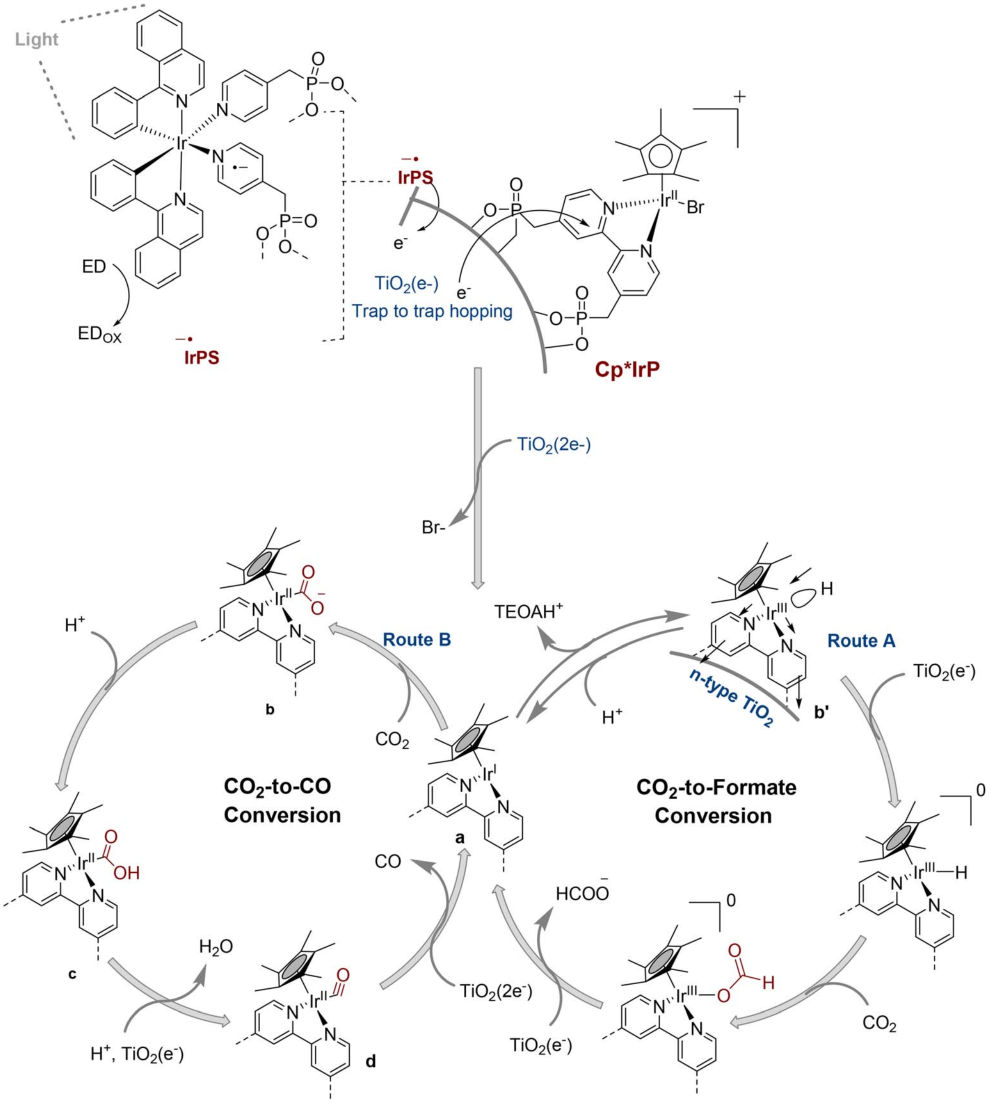

Scheme 11 Photocatalytic pathways enabled by TiO_2 heterogenization of Cp*IrP in a three-component hybrid architecture.

single-atom catalysis.[163,164] In SAA catalysts, the two metal elements can participate in distinct elementary steps of the catalytic process, thereby disrupting the scaling and Brønsted–Evans–Polanyi (BEP) relationships typical of single-metal catalysts and ultimately enhancing the overall reaction.[165,166] Moreover, the geometric and electronic structures of the guest and host metals in SAA can be mutually tuned,[167] thereby modulating the adsorption strength of intermediates and altering the CO_2RR reaction pathway. Such adjustments ultimately enhance the intrinsic activity and selectivity of metal catalysts. For instance, dispersing single Sb atoms onto a Cu surface decreases the adsorption energy of CO by approximately 0.1 eV, while simultaneously increasing the faradaic efficiency for CO from 40% to nearly 90% at a constant current density of 400 mA cm^{-2}.[168] Among metal catalysts, Cu stands out for its unique selectivity in CO_2RR, as it can generate both C_1 and C_{2+} products such as CO, formate, ethylene, ethanol, and propanol.[169] Consequently, Cu-based SAA catalysts have been widely investigated to steer the activity and selectivity of CO_2RR toward the desired products.[170,171]

Zhi *et al.*[172] used DFT to study Cu(111)-supported single-atom alloy (M@Cu) catalysts for CO_2 electroreduction. They showed that the H and O affinities of the single-atom metal M effectively predict CO_2RR selectivity. As shown in Fig. 9A, Ag-, Zn-, In-, and Sn-doped M@Cu catalysts with weak M–H and M–O affinities mainly produce CO and HCOOH, whereas those with strong affinities favor CH_4 or CH_3OH formation.[173] Catalysts with strong M–H but weak M–O affinities are uniquely capable of generating C_2 products. This theoretical selectivity map is consistent with experimental observations; for instance, Cu–In and Cu–Sn alloy electrocatalysts have been shown to preferentially produce CO and HCO_2H.[174–177] Cu–Pt nanocrystals with precisely controlled Cu/Pt ratios exhibited high faradaic efficiency toward CH_4.[178] Cu–Pd and Cu–Au alloy catalysts demonstrated high selectivity for C_2 products.[179–181] The CO_2RR selectivity of SAAs can be effectively described using the M–O and M–H affinities, which further show a correlation with the d-band center of various SAAs (Fig. 9B). Lu *et al.* proposed a SAA catalyst, Co@Cu, capable of selective and efficient methanol production at low overpotential.[182] On the Cu–Co interface, CO* is weakly adsorbed, facilitating its desorption and subsequent product formation. Additionally, the incorporation of Co single atoms modifies the electronic structure of Cu. Particularly, by tuning the d-band, CO_2 reduction to methanol is promoted. The narrowed Co d-band enhances bonding with key intermediates, eliminating the need for their migration and enabling selective and efficient methanol formation *via* the pathway: $CO_2 \rightarrow COOH^* \rightarrow CO^* \rightarrow COH^* \rightarrow CHOH^* \rightarrow CH_2OH^* \rightarrow CH_3OH$.

Although noble metals like gold and silver exhibit high selectivity for converting CO_2 to CO, Cu-based SAAs are often preferred. First, Cu-based catalysts bind *H relatively weakly (weaker than Pt or Pd), which suppresses the HER and enhances the CO_2RR selectivity. Second, the adsorption of key CO_2RR intermediates, such as *CO and *COOH, is moderate on Cu-based catalysts, which allows for efficient rapid *CO desorption and CO_2 activation. Additionally, Cu is more cost-effective than Au and Ag, making it particularly attractive for industrial applications.[183–185] Besides CO, formate ($HCOO^-$) and formic acid (HCO_2H) are important C_1 products of CO_2 electroreduction. However, Cu shows low selectivity for formic acid or formate, and the HER can compete within certain potential ranges. Consequently, steering Cu-based CO_2RR toward formate production remains a significant challenge.[186–188] For instance, Zheng *et al.* reported a Pb SAA Cu catalyst (Pb_1Cu) designed for selective CO_2-to-formic acid conversion with record-high activity. The catalyst was synthesized *in situ* by reducing a Cu–Pb precursor under constant current. Electrochemical tests in a flow cell confirmed the catalyst's high selectivity and activity for formate production.[189] Methane is a primary component of natural gas which is the most reduced product of CO_2RR, requiring an eight-electron transfer. However, the poor selectivity and high overpotential of Cu catalysts for CO_2-to-CH_4 conversion limit their practical application. One effective strategy to enhance CH_4 selectivity on Cu is

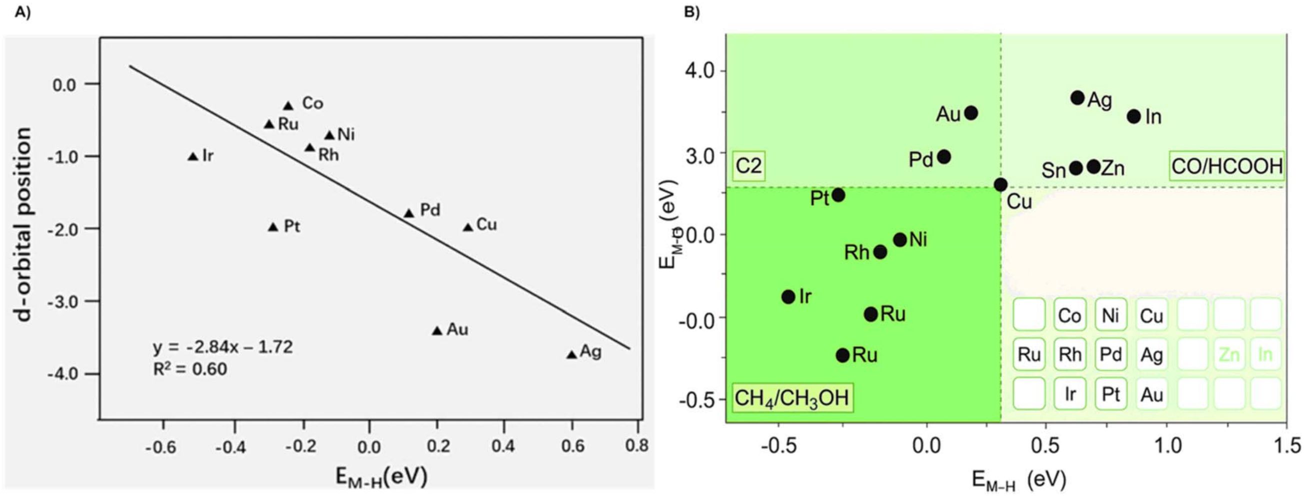

Fig. 9 (A) Classification of the products from M@Cu catalysts based on their affinities for M–H and M–O bonds; (B) correlation between the d-band center of the d-block metal and the M–H bond affinity in the M@Cu catalysts.

to suppress CO* desorption and promote its further protonation.[173] As the only metal capable of reducing CO_2 to multicarbon products, Cu-based materials are being extensively studied for the selective production of C_{2+} compounds.[190,191] C–C coupling is the key step in generating C_{2+} products during CO_2RR. For instance, Zhang *et al.* designed Cu-hosted SAAs with adjacent binary sites that facilitate asymmetric CO binding, thereby enhancing C–C coupling and promoting multicarbon product formation.[192]

Apart from Cu, other metals are also important in CO_2RR. For instance, noble metals like Ag and Au display strong selectivity toward CO, and their catalytic efficiency can be greatly improved by incorporating single-atom alloying.[193–197] Wang *et al.* investigated the surface reconstruction of Ag-supported Cu SAA catalysts during electrochemical CO_2 reduction.[198] Certain metals, including Bi-, Sn-, and Pb-based catalysts, are capable of catalyzing the electroreduction of CO_2 to formic acid or formate.[199]

5. Dual-atom alloys for CO_2RR

In recent years, dual-atom catalysts (DACs), regarded as an important extension of single-atom catalysts (SACs), have attracted growing interest for CO_2 reduction reactions. These catalysts feature bimetallic active sites created by positioning a secondary metal center near the primary metal center.[200] Compared with SACs, DACs not only retain the merits of single-atom catalysts, but also introduce additional functionalities. Their unique coordination environment offers a distinct advantage in regulating the adsorption and desorption behavior of reactants.[201] In addition, the interplay between the two metal atoms in DACs helps tune the electronic structure around the bimetallic active sites.[202] Third, the interaction between the two metal atoms in DACs gives rise to a synergistic effect,[203] which not only enhances the overall catalytic performance, but also enables these catalysts to facilitate more complex chemical reactions.[204] Beyond these advantages, DACs also display a spacing effect. When the two metal atoms are positioned in close proximity, their interaction disrupts the linear scaling relationship of intermediate adsorption energies and lowers the activation barrier, thereby markedly boosting the catalytic efficiency.[205] Thanks to these advantages, DACs have found growing applications in CO_2 reduction. For instance, Zhao *et al.* reported a DAC (Fe_2NPC) constructed by anchoring Fe_2N_6 bimetallic sites onto nitrogen-doped porous carbon. This catalyst achieved a faradaic efficiency of 96.0% for CO, notably higher than the 83.5% obtained with the single-metal counterpart Fe_1NPC.[206] The outstanding electrocatalytic activity of Fe_2NPC is attributed to its Fe–Fe dual active sites, which can simultaneously coordinate with the C and O atoms of CO_2, thereby promoting its activation. Similarly, Wang *et al.* synthesized both Co-based DACs and SACs for the photocatalytic reduction of CO_2 to CH_4, where the DACs exhibited superior selectivity toward CH_4 compared to their single-atom counterparts.[207] Building on these advantages, DACs clearly hold great promise as highly effective catalysts for CO_2 reduction.

5.1. CO_2 adsorption

The CO_2 reduction reaction involves several fundamental stages, including CO_2 diffusion, adsorption, activation, intermediate generation, and final product desorption.[208] The adsorption of CO_2 molecules on the catalyst surface represents a fundamental prerequisite for the initiation of CO_2RR. The strength and capacity of adsorption not only regulate the local concentration of reactants, but also modulate the binding configuration of CO_2, thereby influencing the activation pathway, turnover frequency, and ultimately the overall reaction kinetics and selectivity.[209] Previous studies have shown that CO_2 may adsorb onto the catalyst surface either through physisorption in a linear configuration or *via* chemisorption as a partially charged $CO_2^{\delta\cdot-}$ species through interactions with surface atoms.[210] During chemisorption, interactions between the catalyst surface atoms and the CO_2 molecule induce repulsion between the C and O atoms, leading to a bent molecular configuration.[211] To date, four possible coordination modes of CO_2 molecules on catalyst surfaces have been proposed.[212,213] The first proposed mode is a linear adsorption structure, in which the O atom acts as an electron acceptor and binds to the catalyst surface (Fig. 10a). The second is the C-coordination model, where the C atom interacts with the catalyst to form a monodentate carbonate species (Fig. 10b). The third is the O-coordination model, characterized by the interaction of both O atoms in the CO_2 molecule with the catalyst, leading to the formation of a bridged carbonate structure (Fig. 10c). The fourth is the C/O mixed-coordination model, in which both the C and O atoms simultaneously interact with the catalyst surface to generate a bidentate carbonate species (Fig. 10d). Unlike the linear CO_2 molecule, the chemisorbed $CO_2^{\delta\cdot-}$ species adopts a bent configuration, which lowers the barrier for electron acceptance, since the energy level of its lowest unoccupied molecular orbital decreases upon bending.

5.2. CO_2 activation

The conversion of CO_2 is a highly complex process, involving multistep reaction pathways that generate a variety of intermediates and final products. As previously described, CO_2 molecules are first adsorbed onto the active sites of the catalyst. These adsorbed molecules are then activated *via* electron transfer and further protonated by nearby protons or proton–electron pairs, leading to the formation of various intermediates. The final products subsequently desorb from the active sites and diffuse away from the catalyst surface, either into the electrolyte or back into the bulk gas phase. A wide range of CO_2 reduction products can be obtained, including formate, CO, methanol, methane, ethylene, ethanol, and syngas.[214–216] This diversity arises because different CO_2 adsorption configurations influence the reaction pathways, generating distinct intermediates and thereby affecting product selectivity. For instance, in the C-coordination model, when the C atom interacts with a Lewis base center on the catalyst to form a monodentate carbonate species, it promotes the formation of the carboxyl radical ($^{\bullet}COOH$).[217] However, when the two O atoms interact with the catalyst surface to form a bidentate carbonate species,

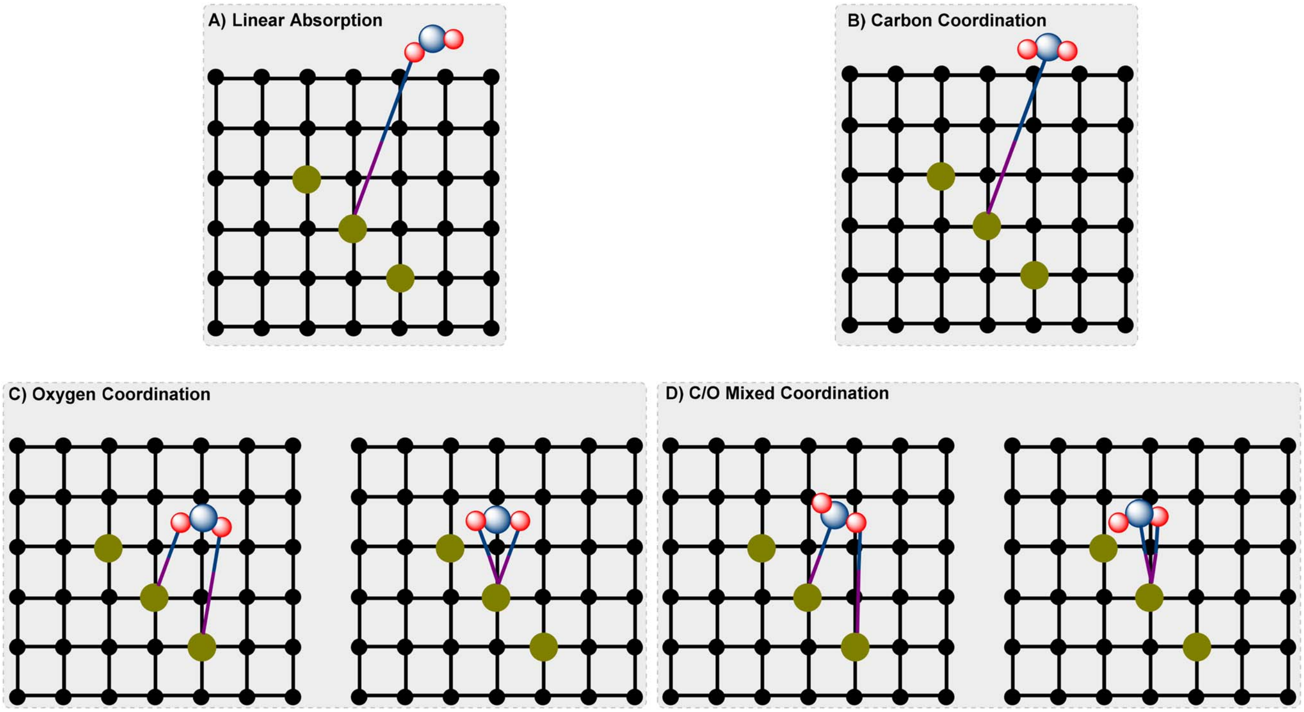

Fig. 10 Adsorption modes of CO_2 molecules on catalytic surfaces.

hydrogen atoms preferentially attach to the C atom of $CO_2^{\delta\bullet-}$, leading to the formation of a formate anion bound to the catalyst surface in a bidentate configuration.[218] In addition, from a thermodynamic perspective, CO_2 is relatively stable due to its linear structure and chemical inertness. The C=O bonds in CO_2 are particularly difficult to cleave, possessing a high dissociation energy of 750 kJ mol^{-1}.[66]

6. MOF-derived CO_2RR

Metal–organic frameworks (MOFs) represent a new class of crystalline porous materials formed by the coordination of inorganic nodes such as metal ions or clusters with organic linkers.[6,219–221] Owing to the structural diversity and tunable composition of MOFs, pore sizes can be adjusted and a variety of catalytic sites can be introduced by manipulating the inorganic nodes and organic linkers. Their porous architecture and large surface areas facilitate improved CO_2 adsorption and efficient mass transport. In addition, the well-defined framework of MOFs provides a valuable platform for exploring the structure–property relationships and mechanistic studies. MOF-derived materials have emerged as versatile catalysts for both electrocatalytic and photocatalytic CO_2 reduction, building on Fischer's pioneering work with NH_2-MIL-125-derived TiO_2,[222] while most reviews broadly cover MOFs, composites, and derived materials, and photocatalytic applications.[223–229] Optimizing the morphology and electronic structure of MOF-derived catalysts for both electrocatalysis and photocatalysis can therefore unlock new strategies for enhanced CO_2 conversion.[6]

Due to its closed-shell electronic configuration, CO_2 is chemically inert and thermodynamically stable, with a bond dissociation energy of 750 kJ mol^{-1}.[230,231] Therefore, efficient electrocatalysts and photocatalysts are necessary to overcome these thermodynamic and kinetic barriers, and convert CO_2 into value-added products such as HCOOH, CO and CH_4. MOF-derived materials, with their tunable structures, high surface areas, and adjustable catalytic sites, provide a promising platform to facilitate CO_2 activation and enhance the efficiency of both photocatalytic and electrocatalytic conversion processes.

In both photocatalytic and electrocatalytic CO_2 reduction reactions, CO_2 molecules are initially activated to form the $^*CO_2^-$ intermediate, requiring a negative reduction potential of −1.90 V *versus* the normal hydrogen electrode (NHE). The subsequent reduction of this intermediate, determined by the number of electrons transferred and protons added, leads to a variety of products, including two-electron reduction products such as CO and HCOOH, as well as multi-electron products like CH_4, CH_3OH and C_2H_5OH.[232] In general, the $^*CO_2^-$ intermediate undergoes protonation to produce either the *OCHO or *COOH intermediate. The *OCHO intermediate can be further reduced to form formic acid, whereas *COOH proceeds to generate the *CO intermediate, which can then lead to C_1 products (HCHO, CH_4, CH_3OH, CO) and C_{2+} products (C_2H_5OH, C_2H_4, C_3H_7OH, CH_3CO_2H). Typically, C–C bond formation occurs more slowly than the hydrogen evolution reaction (HER), which results in lower selectivity toward C_{2+} products.[233] Enhancing the conversion of the *CO intermediate into the desired C_{2+} products requires a sufficiently strong interaction between *CO and the catalytic site. However, excessively strong binding can lead to catalyst “poisoning,” as the desorption of *CO becomes difficult, ultimately reducing the overall catalytic activity.[223,233,234] The standard redox potentials for hydrogen evolution and CO_2 reduction to various products are comparable, which promotes the competing HER. In addition, the redox potentials among different CO_2 reduction products are similar, often resulting in the formation of mixed products and limiting selectivity toward a single desired product.[232] Consequently, minimizing side reactions and enhancing product selectivity are key factors to consider in the design of effective CO_2 reduction catalysts.

Electrocatalytic CO_2 reduction involves three main steps: (i) adsorption of CO_2 onto the catalyst surface, (ii) electron transfer and proton migration to the adsorbed CO_2, and (iii) structural rearrangement of intermediates, followed by desorption of the final products from the catalyst surface.[6] Electrocatalytic CO_2 reduction typically requires a significant overpotential, the difference between the equilibrium potential and the applied potential to enable CO_2 molecules to accept electrons and form the $*CO_2^-$ intermediate. Depending on the type of electrocatalyst and experimental conditions, the reaction can follow multiple pathways, yielding a variety of reduction products (Fig. 11). Due to the similar reduction potentials of CO_2 products and the kinetically favorable HER, achieving high selectivity for a single product remains a major challenge. The rational design of catalyst morphologies can modulate key parameters, including exposed surface area, mass transport, and charge-transfer resistance, thereby enhancing the catalytic activity and steering product selectivity.[235,236] By tuning the electronic structure of catalysts, the binding strength of the reaction intermediates can be adjusted, which in turn influences the reaction barriers and dictates the distribution of the reduction products.[237]

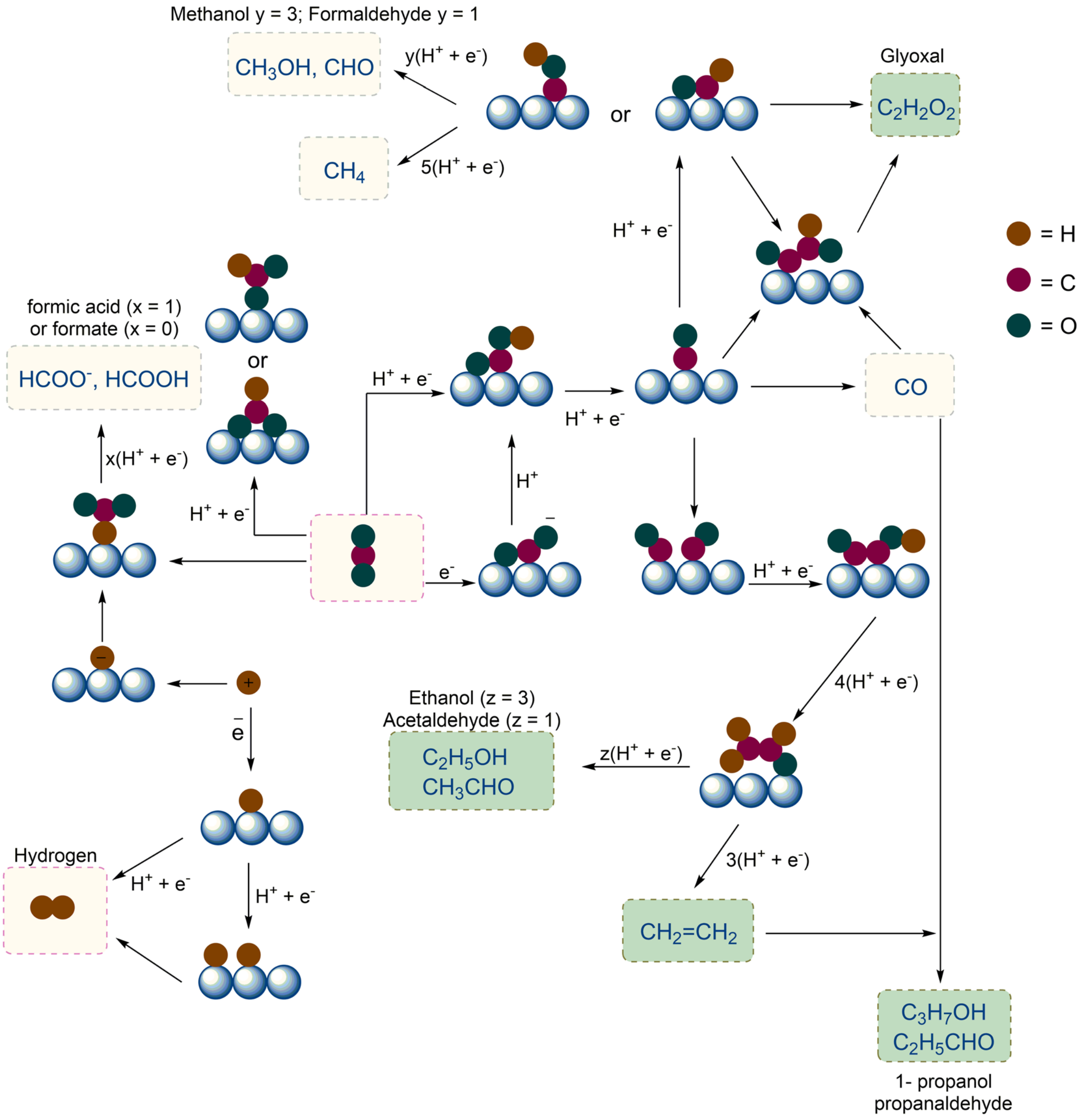

Fig. 11 Schematic reaction pathways for CO_2 reduction by MOF.

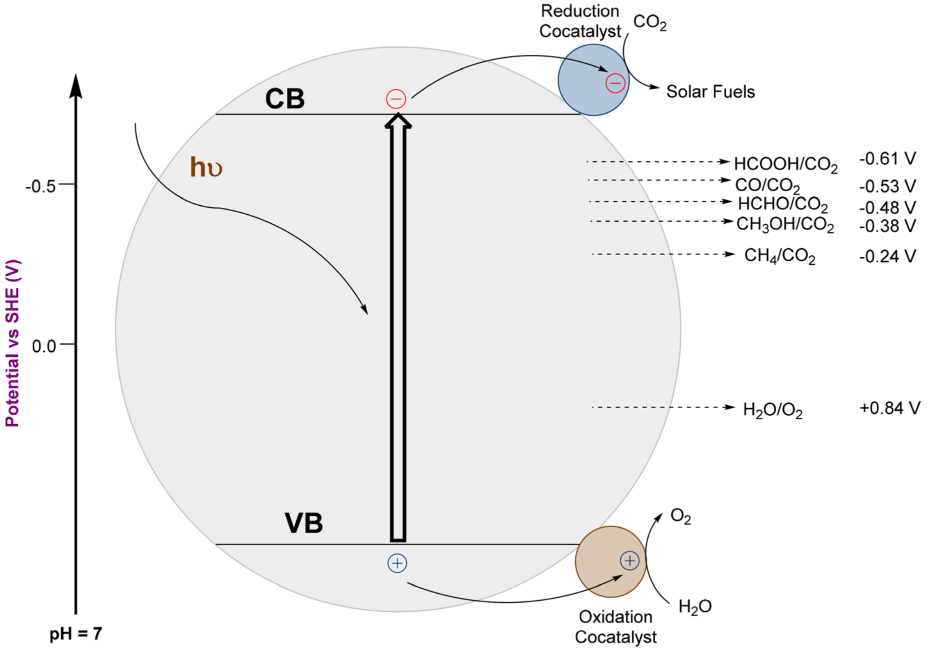

Fig. 12 Photocatalytic CO_2 reduction on a semiconductor photocatalyst.

In photocatalytic CO_2 reduction, the reaction is generally considered to proceed through three primary steps: (i) photoexcitation of the catalyst to generate electron–hole pairs (e^-–h^+), (ii) migration of the photogenerated electrons and holes to the catalyst surface, and (iii) reduction of CO_2 on the catalyst surface (Fig. 12).[19,238] Unlike electrocatalysis, photocatalysis requires the conversion of light energy into excited electrons and holes to drive chemical reactions. Therefore, the ability of a photocatalyst to absorb light efficiently and separate charge carriers effectively is crucial. When the photocatalyst absorbs photons with energy equal to or greater than its bandgap, electrons are promoted from the valence band (VB) to the conduction band (CB), leaving holes in the VB and generating electron–hole pairs.[6] The redox capabilities of photogenerated electrons and holes in photocatalysts are largely determined by the positions of the conduction band minimum (CBM) and valence band maximum (VBM), respectively. CO_2 reduction can proceed only when the CBM energy lies at a more negative potential than the redox potential of the CO_2RR.[238,239] Similarly, VBM must be positioned at a more positive potential than the redox potential of the oxidation half-reaction; otherwise, sacrificial agents such as triethanolamine (TEOA), ascorbic acid, or lactic acid are required to serve as alternative electron donors. Careful design of the catalyst's morphology and electronic structure can significantly improve light absorption. In particular, tuning the catalyst's thickness and surface features influences the light penetration depth and scattering intensity, thereby enhancing the overall light-harvesting efficiency. Moreover, the electronic structure of a material directly affects its energy level distribution, enabling the absorption of longer-wavelength light and thereby enhancing the efficiency of light utilization.

The second step involves the separation of photogenerated electron–hole pairs and their migration to the catalyst surface. For effective CO_2 reduction, these charge carriers must have a sufficiently long lifetime to reach the active sites. However, this process is often hindered by the recombination of electrons and holes, which significantly reduces the utilization efficiency of the photogenerated charges.[240] By tailoring the morphology and electronic structure of catalysts, the charge-transfer distance can be reduced and the lifetime of photogenerated carriers extended, thereby suppressing the recombination of electrons and holes.[241] To enhance the separation efficiency of charge carriers, strategies such as constructing heterojunctions and improving the crystallinity of the materials have been widely adopted.[242,243] Similar to electrocatalysis, the surface redox reaction is a crucial step in photocatalysis. When photogenerated electrons reach the active sites, the adsorbed CO_2 molecules undergo reduction. Introducing CO_2 binding sites on the catalyst surface can enhance CO_2 enrichment and thereby improve catalytic performance. Additionally, tuning the coordination environment of active sites helps stabilize key intermediates and lowers the reaction barrier of the rate-determining step (RDS). To further enhance the surface reaction efficiency, strategies such as incorporating co-catalysts and creating surface defects are commonly employed.[6,244,245]

7. Conclusion

The electrochemical and photocatalytic reduction of CO_2 represents a pivotal strategy for addressing rising carbon emissions, while generating value-added fuels and chemicals. Across homogeneous, heterogeneous, and hybrid platforms, recent advances underscore the importance of understanding and controlling the fundamental steps of CO_2 activation, intermediate stabilization, and product selectivity. Key insights show that product selectivity is dictated by how catalysts stabilize CO_2, hydride, and *COOH intermediates, and how effectively competing hydrogen evolution is suppressed. Photocatalytic systems complement electrocatalysis by coupling solar energy capture with catalytic turnover. Hybrid molecular–inorganic–organic assemblies, particularly TiO_2-anchored complexes, illustrate how site isolation and semiconductor–molecule coupling suppress deactivation, reshape hydricity, and even enable tunable syngas generation. At the materials frontier, single-atom and dual-atom alloys, alongside MOF-derived catalysts, are redefining heterogeneous CO_2RR. Single-atom alloys (SAAs) disrupt scaling relations by electronically coupling isolated guest atoms with host metals, offering precise control over *CO binding and C–C coupling pathways. Dual-atom catalysts (DACs) further introduce synergistic bimetallic effects, stabilizing bent $CO_2^{\delta-}$ intermediates and enabling complex multi-electron conversions with higher selectivity than SACs alone. Meanwhile, MOF-derived catalysts provide high surface area, tunable coordination environments, and structural porosity that enhance CO_2 adsorption and diffusion, enabling both C_1 and C_{2+} products. These platforms collectively illustrate how structural precision and compositional tuning can directly translate into reactivity and selectivity gains. Future progress will depend on uniting mechanistic insight, second-sphere tuning, and advanced material architectures to deliver efficient, durable, and practical CO_2 conversion technologies.

Data availability

Not applicable.

Conflicts of interest

There are no conflicts to declare.

References

1 J. Cheon, J. Y. Yang, M. Koper and O. Ishitani, *Acc. Chem. Res.*, 2022, **55**, 931–932.

2 H.-J. Son, C. Pac and S. O. Kang, *Acc. Chem. Res.*, 2021, **54**, 4530–4544.

3 M. Halmann, *Nature*, 1978, **275**, 115–116.

4 Z. Chen, J. Xiong and G. Cheng, *Fuel*, 2024, **357**, 129806.

5 M. Khan, Z. Akmal, M. Tayyab, S. Mansoor, A. Zeb, Z. Ye, J. Zhang, S. Wu and L. Wang, *Carbon Capture Sci. Technol.*, 2024, **11**, 100191.

6 Y.-T. Zheng, S. Li, N.-Y. Huang, X. Li and Q. Xu, *Coord. Chem. Rev.*, 2024, **510**, 215858.

7 H. Wang, X. Kang and B. Han, *ChemSusChem*, 2024, **17**, e202301539.

8 W. Xu, H. Shang, J. Guan, X. Yang, X. Jin, L. Tao and Z. Shao, *Adv. Funct. Mater.*, 2025, **35**, 2412812.

9 H. Wang, X. Kang and B. Han, *ChemSusChem*, 2024, **17**, e202301539.

10 W. Xu, H. Shang, J. Guan, X. Yang, X. Jin, L. Tao and Z. Shao, *Adv. Funct. Mater.*, 2025, **35**, 2412812.

11 J. Barber, *Chem. Soc. Rev.*, 2009, **38**, 185–196.

12 G. W. Crabtree and N. S. Lewis, *Phys. Today*, 2007, **60**, 37–42.

13 M. Aresta, A. Dibenedetto and A. Angelini, *Chem. Rev.*, 2014, **114**, 1709–1742.

14 S. Chu, Y. Cui and N. Liu, *Nat. Mater.*, 2017, **16**, 16–22.

15 M. D. Doherty, D. C. Grills, J. T. Muckerman, D. E. Polyansky and E. Fujita, *Coord. Chem. Rev.*, 2010, **254**, 2472–2482.

16 J.-M. Savéant, *Chem. Rev.*, 2008, **108**, 2348–2378.

17 E. E. Benson, C. P. Kubiak, A. J. Sathrum and J. M. Smieja, *Chem. Soc. Rev.*, 2009, **38**, 89–99.

18 F. Franco, C. Rettenmaier, H. S. Jeon and B. Roldan Cuenya, *Chem. Soc. Rev.*, 2020, **49**, 6884–6946.

19 E. V. Kondratenko, G. Mul, J. Baltrusaitis, G. O. Larrazábal and J. Pérez-Ramírez, *Energy Environ. Sci.*, 2013, **6**, 3112–3135.

20 N. Elgrishi, M. B. Chambers, X. Wang and M. Fontecave, *Chem. Soc. Rev.*, 2017, **46**, 761–796.

21 A. Xu, N. Govindarajan, G. Kastlunger, S. Vijay and K. Chan, *Acc. Chem. Res.*, 2022, **55**, 495–503.

22 S. Overa, B. H. Ko, Y. Zhao and F. Jiao, *Acc. Chem. Res.*, 2022, **55**, 638–648.

23 S. Cherukuri, S. Chaubey and V. Chaubey, *Vietnam J. Chem.*, 2025, 1.

24 Z. Qiuting and W. Wenguang, *Chin. J. Org. Chem.*, 2024, **44**, 3106.

25 M. Sain, D. Dey, R. Sen and S. Chowdhury, *RSC Sustainability*, 2025, **3**, 2733–2749.

26 Y. Jiang, S. Li, Y. Fan and Z. Tang, *Angew. Chem.*, 2024, **136**, e202404658.

27 J. Tian, Y. Sun, Y. Wu, F. Wang, Y. Zhang, D. Fu, Z. Chen and X. Wang, *J. Mater. Chem. A*, 2025, **13**, 21268–21291.

28 G. Wang, J. Chen, Y. Ding, P. Cai, L. Yi, Y. Li, C. Tu, Y. Hou, Z. Wen and L. Dai, *Chem. Soc. Rev.*, 2021, **50**, 4993–5061.

29 S. Zhai, J. Rojas, N. Ahlborg, K. Lim, C. H. M. Cheng, C. Xie, M. F. Toney, I.-H. Jung, W. C. Chueh and A. Majumdar, *Energy Environ. Sci.*, 2020, **13**, 592–600.

30 J. M. Naik, C. Ritter, B. Bulfin, A. Steinfeld, R. Erni and G. R. Patzke, *Adv. Energy Mater.*, 2021, **11**, 2003532.

31 K. Schlenker, E. G. Christensen, A. A. Zhanserkeev, G. R. McDonald, E. L. Yang, K. T. Lutz, R. P. Steele, R. T. VanderLinden and C. T. Saouma, *ACS Catal.*, 2021, **11**, 8358–8369.

32 Z. Lei, Y. Xue, W. Chen, W. Qiu, Y. Zhang, S. Horike and L. Tang, *Adv. Energy Mater.*, 2018, **8**, 1801587.

33 Z. Liu, L.-F. Wu, C. L. Kufner, D. D. Sasselov, W. W. Fischer and J. D. Sutherland, *Nat. Chem.*, 2021, **13**, 1126–1132.

34 J. Xu, Z. Ju, W. Zhang, Y. Pan, J. Zhu, J. Mao, X. Zheng, H. Fu, M. Yuan, H. Chen and R. Li, *Angew. Chem., Int. Ed.*, 2021, **60**, 8705–8709.

35 F. M. Schwarz, J. Moon, F. Oswald and V. Müller, *Joule*, 2022, **6**, 1304–1319.

36 N. Briggs, G. Dall'Olmo and H. Claustre, *Science*, 2020, **367**, 791–793.

37 S. Luo, P. P. Lin, L.-Y. Nieh, G.-B. Liao, P.-W. Tang, C. Chen and J. C. Liao, *Nat. Catal.*, 2022, **5**, 154–162.

38 H.-Q. Liang, T. Beweries, R. Francke and M. Beller, *Angew. Chem., Int. Ed.*, 2022, **61**, e202200723.

39 C. Park, S. Lee and J. Lee, *Chem. Eng. J.*, 2022, **427**, 131459.

40 Q. Zhi, J. Zhou, W. Liu, L. Gong, W. Liu, H. Liu, K. Wang and J. Jiang, *Small*, 2022, **18**, 2201314.

41 J. Zhao, M. Ji, H. Chen, Y.-X. Weng, J. Zhong, Y. Li, S. Wang, Z. Chen, J. Xia and H. Li, *Appl. Catal., B*, 2022, **307**, 121162.

42 Y. H. Kim, N. Kim, J.-M. Seo, J.-P. Jeon, H.-J. Noh, D. H. Kweon, J. Ryu and J.-B. Baek, *Chem. Mater.*, 2021, **33**, 8705–8711.

43 X. Shi, P. An, Q. Zhang, Q. Song, D. Jiang, D. Tian and D. Li, *Chem. Eng. J.*, 2022, **446**, 137096.

44 S. Monticelli, A. Talbot, P. Gotico, F. Caillé, O. Loreau, A. Del Vecchio, A. Malandain, A. Sallustrau, W. Leibl, A. Aukauloo, F. Taran, Z. Halime and D. Audisio, *Nat. Commun.*, 2023, **14**, 4451.

45 T. Inoue, A. Fujishima, S. Konishi and K. Honda, *Nature*, 1979, **277**, 637–638.

46 Ž. Kovačič, B. Likozar and M. Huš, *ACS Catal.*, 2020, **10**, 14984–15007.

47 C. Costentin, M. Robert and J.-M. Savéant, *Acc. Chem. Res.*, 2015, **48**, 2996–3006.

48 I. Azcarate, C. Costentin, M. Robert and J.-M. Savéant, *J. Phys. Chem. C*, 2016, **120**, 28951–28960.

49 Z. Masood and Q. Ge, *Molecules*, 2023, **28**, 375.

50 B. Mondal, A. Rana, P. Sen and A. Dey, *J. Am. Chem. Soc.*, 2015, **137**, 11214–11217.

51 S. Dey, M. E. Ahmed and A. Dey, *Inorg. Chem.*, 2018, **57**, 5939–5947.

52 B. Mondal, P. Sen, A. Rana, D. Saha, P. Das and A. Dey, *ACS Catal.*, 2019, **9**, 3895–3899.

53 S. Amanullah, P. Saha and A. Dey, *J. Am. Chem. Soc.*, 2021, **143**, 13579–13592.

54 Y. Shen, N. Fang, X. Liu, Y. Ling, Y. Su, T. Tan, F. Chen, H. Lin, B. Zhao, J. Wang, D. Si, S. Xie, Y. Wang, D. Zhou, T. Zhang, R. Cao and C. Wang, *Nat. Commun.*, 2025, **16**, 2073.

55 S. Wang, F. Li, J. Zhao, Y. Zeng, Y. Li, Z.-Y. Lin, T.-J. Lee, S. Liu, X. Ren, W. Wang, Y. Chen, S.-F. Hung, Y.-R. Lu, Y. Cui, X. Yang, X. Li, Y. Huang and B. Liu, *Nat. Commun.*, 2024, **15**, 10247.

56 A. Singh, S. Barman, F. A. Rahimi, A. Dey, R. Jena, R. Kumar, N. Mathew, D. Bhattacharyya and T. K. Maji, *Energy Environ. Sci.*, 2024, **17**, 2315–2325.

57 Y. Zhao, Q. Yuan, R. Xu, C. Zhang, K. Sun, A. Wang, A. Zhang, Z. Wang, J. Jiang and M. Fan, *Appl. Catal., B*, 2024, **355**, 124168.

58 M. A. Z. G. Sial, N. Guo, A. Jalil, M. Abbas, M. Mateen, S. Ullah, U. Alam, Z. M. Bhat, A. Hussain, X. Cai and P. Tsiakaras, *Chem. Eng. J.*, 2024, **489**, 151099.

59 Y. Chen, X.-Y. Li, Z. Chen, A. Ozden, J. E. Huang, P. Ou, J. Dong, J. Zhang, C. Tian, B.-H. Lee, X. Wang, S. Liu, Q. Qu, S. Wang, Y. Xu, R. K. Miao, Y. Zhao, Y. Liu, C. Qiu, J. Abed, H. Liu, H. Shin, D. Wang, Y. Li, D. Sinton and E. H. Sargent, *Nat. Nanotechnol.*, 2024, **19**, 311–318.

60 N. Dhabarde, J. Selvaraj, A. Yuda, A. Kumar and V. R. Subramanian, *Int. J. Hydrogen Energy*, 2022, **47**, 30908–30936.

61 H. Dang, B. Guan, L. Zhu, J. Chen, Z. Zhuang, Z. Ma, X. Hu, C. Zhu, S. Zhao, K. Shu, J. Gao, L. Zhang, T. Zhu and Z. Huang, *Energy Fuels*, 2025, **39**, 10109–10133.

62 H. Pan and M. D. Heagy, *Nanomaterials*, 2020, **10**, 2422.

63 E. E. Benson, C. P. Kubiak, A. J. Sathrum and J. M. Smieja, *Chem. Soc. Rev.*, 2009, **38**, 89–99.

64 S. Amanullah, P. Saha, A. Nayek, M. E. Ahmed and A. Dey, *Chem. Soc. Rev.*, 2021, **50**, 3755–3823.

65 A. M. Appel, J. E. Bercaw, A. B. Bocarsly, H. Dobbek, D. L. DuBois, M. Dupuis, J. G. Ferry, E. Fujita, R. Hille and P. J. Kenis, *Chem. Rev.*, 2013, **113**, 6621–6658.

66 R. Francke, B. Schille and M. Roemelt, *Chem. Rev.*, 2018, **118**, 4631–4701.

67 A. Khadhraoui, P. Gotico, B. Boitrel, W. Leibl, Z. Halime and A. Aukauloo, *Chem. Commun.*, 2018, **54**, 11630–11633.

68 D. J. Martin and J. M. Mayer, *J. Am. Chem. Soc.*, 2021, **143**, 11423–11434.

69 S. Sung, D. Kumar, M. Gil-Sepulcre and M. Nippe, *J. Am. Chem. Soc.*, 2017, **139**, 13993–13996.

70 S. Sung, X. Li, L. M. Wolf, J. R. Meeder, N. S. Bhuvanesh, K. A. Grice, J. A. Panetier and M. Nippe, *J. Am. Chem. Soc.*, 2019, **141**, 6569–6582.

71 I. Azcarate, C. Costentin, M. Robert and J.-M. Savéant, *J. Am. Chem. Soc.*, 2016, **138**, 16639–16644.

72 E. M. Nichols, J. S. Derrick, S. K. Nistanaki, P. T. Smith and C. J. Chang, *Chem. Sci.*, 2018, **9**, 2952–2960.

73 P. Sen, B. Mondal, D. Saha, A. Rana and A. Dey, *Dalton Trans.*, 2019, **48**, 5965–5977.

74 P. Gotico, B. Boitrel, R. Guillot, M. Sircoglou, A. Quaranta, Z. Halime, W. Leibl and A. Aukauloo, *Angew. Chem., Int. Ed.*, 2019, **58**, 4504–4509.

75 F. Franco, S. Fernandez and J. Lloret-Fillol, *Curr. Opin. Electrochem.*, 2019, **15**, 109–117.

76 A. W. Nichols and C. W. Machan, *Front. Chem.*, 2019, **7**, 397.

77 P. Gotico, Z. Halime and A. Aukauloo, *Dalton Trans.*, 2020, **49**, 2381–2396.

78 S. Amanullah, P. Saha and A. Dey, *J. Am. Chem. Soc.*, 2021, **143**, 13579–13592.

79 X. She, L. Zhai, Y. Wang, P. Xiong, M. M.-J. Li, T.-S. Wu, M. C. Wong, X. Guo, Z. Xu, H. Li, H. Xu, Y. Zhu, S. C. E. Tsang and S. P. Lau, *Nat. Energy*, 2024, **9**, 81–91.

80 G. L. Gutsev, R. J. Bartlett and R. N. Compton, *J. Chem. Phys.*, 1998, **108**, 6756–6762.

81 S. Mukhopadhyay, M. S. Naeem, G. Shiva Shanker, A. Ghatak, A. R. Kottaichamy, R. Shimoni, L. Avram, I. Liberman, R. Balilty, R. Ifraemov, I. Rozenberg, M. Shalom, N. López and I. Hod, *Nat. Commun.*, 2024, **15**, 3397.

82 Z.-M. Zhang, T. Wang, Y.-C. Cai, X.-Y. Li, J.-Y. Ye, Y. Zhou, N. Tian, Z.-Y. Zhou and S.-G. Sun, *Nat. Catal.*, 2024, **7**, 807–817.

83 W. Wei, H. Liu and Q.-L. Zhu, *Research*, 2025, **8**, 0589.

84 W. Wu, L. Xu, Q. Lu, J. Sun, Z. Xu, C. Song, J. C. Yu and Y. Wang, *Adv. Mater. Lett.*, 2025, **37**, 2312894.

85 H. Wang, C. Ma, Q. Lu, M. Gu, L. Jiang, Y. Hao, F. Hu, L. Li, G. Wang, S. Peng and X. Zhang, *Angew. Chem., Int. Ed.*, 2025, **64**, e202501091.

86 J. Schneider, H. Jia, J. T. Muckerman and E. Fujita, *Chem. Soc. Rev.*, 2012, **41**, 2036–2051.

87 D. H. Gibson, *Chem. Rev.*, 1996, **96**, 2063–2096.

88 S. Gambarotta, F. Arena, C. Floriani and P. F. Zanazzi, *J. Am. Chem. Soc.*, 1982, **104**, 5082–5092.

89 N. W. Kinzel, C. Werlé and W. Leitner, *Angew. Chem., Int. Ed.*, 2021, **60**, 11628–11686.

90 D. H. Gibson, *Coord. Chem. Rev.*, 1999, **185–186**, 335–355.

91 H. J. Freund and M. W. Roberts, *Surf. Sci. Rep.*, 1996, **25**, 225–273.

92 M. Zhang, M. El-Roz, H. Frei, J. L. Mendoza-Cortes, M. Head-Gordon, D. C. Lacy and J. C. Peters, *J. Phys. Chem. C*, 2015, **119**, 4645–4654.

93 M. D. Sampson and C. P. Kubiak, *J. Am. Chem. Soc.*, 2016, **138**, 1386–1393.

94 S. Amanullah, P. Saha, A. Nayek, M. E. Ahmed and A. Dey, *Chem. Soc. Rev.*, 2021, **50**, 3755–3823.

95 E. M. Nichols, J. S. Derrick, S. K. Nistanaki, P. T. Smith and C. J. Chang, *Chem. Sci.*, 2018, **9**, 2952–2960.

96 P. Saha, S. Amanullah, S. Barman and A. Dey, *J. Am. Chem. Soc.*, 2025, **147**, 1497–1507.

97 B. Bai, Y. Pan, J. Zhao, X.-P. Zhang and R. Cao, *Inorg. Chem.*, 2025, **64**, 4826–4834.

98 J. J. Warren, *Acc. Chem. Res.*, 2024, **57**, 2512–2521.

99 B. X. Nguyen, A. Sonea and J. J. Warren, *Inorg. Chem.*, 2023, **62**, 17602–17611.

100 J. S. Derrick, M. Loipersberger, S. K. Nistanaki, A. V. Rothweiler, M. Head-Gordon, E. M. Nichols and C. J. Chang, *J. Am. Chem. Soc.*, 2022, **144**, 11656–11663.

101 S. Patra, S. Ghosh, S. Samanta, A. Nayek and A. Dey, *J. Organomet. Chem.*, 2025, **1023**, 123439.

102 S. Ghosh, S. Patra, A. Bisoi, S. Ghosh, N. Maurya, A. Das, P. C. Singh and A. Dey, *ACS Catal.*, 2025, **15**, 3595–3610.

103 A. Chapovetsky, M. Welborn, J. M. Luna, R. Haiges, T. F. Miller III and S. C. Marinescu, *ACS Cent. Sci.*, 2018, **4**, 397–404.

104 A. Khadhraoui, P. Gotico, B. Boitrel, W. Leibl, Z. Halime and A. Aukauloo, *Chem. Commun.*, 2018, **54**, 11630–11633.

105 X.-M. Liang, Z.-J. Ruan, G.-Q. Guo, J.-Q. Lin and D.-C. Zhong, *ChemCatChem*, 2025, **17**, e202401394.

106 A. Briš and D. Margetić, *Organics*, 2023, **4**, 277–288.

107 C. Zhu, C. D'Agostino and S. P. de Visser, *Inorg. Chem.*, 2024, **63**, 4474–4481.

108 S. Dey, M. E. Ahmed and A. Dey, *Inorg. Chem.*, 2018, **57**, 5939–5947.

109 C. G. Margarit, N. G. Asimow, C. Costentin and D. G. Nocera, *CS Energy Lett.*, 2020, **5**, 72–78.

110 L. Chen, Z. Guo, X.-G. Wei, C. Gallenkamp, J. Bonin, E. Anxolabéhère-Mallart, K.-C. Lau, T.-C. Lau and M. Robert, *J. Am. Chem. Soc.*, 2015, **137**, 10918–10921.

111 P.-L. Luo, I. Y. Chen, M. A. H. Khan and D. E. Shallcross, *Commun. Chem.*, 2023, **6**, 130.

112 C. Costentin, G. Passard, M. Robert and J.-M. Savéant, *J. Am. Chem. Soc.*, 2014, **136**, 11821–11829.

113 C. Costentin, S. Drouet, M. Robert and J.-M. Savéant, *Science*, 2012, **338**, 90–94.

114 C. G. Margarit, C. Schnedermann, N. G. Asimow and D. G. Nocera, *Organometallics*, 2018, **38**, 1219–1223.

115 A. Huang, T. Zhou, J. Zhang, Y. Zhang, Y. Wu, Y. Wang and W. Luo, *ChemCatChem*, 2024, **16**, e202400504.

116 I. S. Kwon, S. J. Lee, J. Y. Kim, I. H. Kwak, G. M. Zewdie, S. J. Yoo, J.-G. Kim, K.-S. Lee, J. Park and H. S. Kang, *ACS Nano*, 2023, **17**, 2968–2979.

117 J. Feng, L. Zhang, S. Liu, L. Xu, X. Ma, X. Tan, L. Wu, Q. Qian, T. Wu and J. Zhang, *Nat. Commun.*, 2023, **14**, 4615.

118 B. M. Ceballos and J. Y. Yang, *Proc. Natl. Acad. Sci. U. S. A.*, 2018, **115**, 12686–12691.

119 S. Roy, B. Sharma, J. Pécaut, P. Simon, M. Fontecave, P. D. Tran, E. Derat and V. Artero, *J. Am. Chem. Soc.*, 2017, **139**, 3685–3696.

120 J. M. Barlow and J. Y. Yang, *ACS Cent. Sci.*, 2019, **5**, 580–588.

121 K. M. Waldie, A. L. Ostericher, M. H. Reineke, A. F. Sasayama and C. P. Kubiak, *ACS Catal.*, 2018, **8**, 1313–1324.

122 J. D. Froehlich and C. P. Kubiak, *J. Am. Chem. Soc.*, 2015, **137**, 3565–3573.

123 M. E. Ahmed, A. Rana, R. Saha, S. Dey and A. Dey, *Inorg. Chem.*, 2020, **59**, 5292–5302.

124 M. Abdinejad, A. Seifitokaldani, C. Dao, E. H. Sargent, X.-A. Zhang and H. B. Kraatz, *ACS Appl. Energy Mater.*, 2019, **2**, 1330–1335.

125 M. D. Sampson, A. D. Nguyen, K. A. Grice, C. E. Moore, A. L. Rheingold and C. P. Kubiak, *J. Am. Chem. Soc.*, 2014, **136**, 5460–5471.

126 A. D. Cypcar and J. Y. Yang, *Acc. Chem. Res.*, 2024, **57**, 3488–3499.

127 J. Y. Yang, T. A. Kerr, X. S. Wang and J. M. Barlow, *J. Am. Chem. Soc.*, 2020, **142**, 19438–19445.

128 B. M. Ceballos and J. Y. Yang, *Proc. Natl. Acad. Sci. U. S. A.*, 2018, **115**, 12686–12691.

129 D. W. Cunningham, J. M. Barlow, R. S. Velazquez and J. Y. Yang, *Angew. Chem., Int. Ed.*, 2020, **59**, 4443–4447.

130 C. Tsay, B. N. Livesay, S. Ruelas and J. Y. Yang, *J. Am. Chem. Soc.*, 2015, **137**, 14114–14121.

131 S. Fang and Y. H. Hu, *Chem. Soc. Rev.*, 2022, **51**, 3609–3647.

132 K. Li, B. Peng and T. Peng, *ACS Catal.*, 2016, **6**, 7485–7527.

133 Q. Wang, J. Warnan, S. Rodríguez-Jiménez, J. J. Leung, S. Kalathil, V. Andrei, K. Domen and E. Reisner, *Nat. Energy*, 2020, **5**, 703–710.

134 S. Wang, M. Xu, T. Peng, C. Zhang, T. Li, I. Hussain, J. Wang and B. Tan, *Nat. Commun.*, 2019, **10**, 676.

135 Y. Wang, X. Shang, J. Shen, Z. Zhang, D. Wang, J. Lin, J. C. S. Wu, X. Fu, X. Wang and C. Li, *Nat. Commun.*, 2020, **11**, 3043.

136 T. Yan, N. Li, L. Wang, Q. Liu, F. M. Ali, L. Wang, Y. Xu, Y. Liang, Y. Dai, B. Huang, J. You and G. A. Ozin, *Energy Environ. Sci.*, 2020, **13**, 3054–3063.

137 W. Shangguan, Q. Liu, Y. Wang, N. Sun, Y. Liu, R. Zhao, Y. Li, C. Wang and J. Zhao, *Nat. Commun.*, 2022, **13**, 3894.

138 Y. Li, D. Hui, Y. Sun, Y. Wang, Z. Wu, C. Wang and J. Zhao, *Nat. Commun.*, 2021, **12**, 123.

139 X. Zhang, X. Li, D. Zhang, N. Q. Su, W. Yang, H. O. Everitt and J. Liu, *Nat. Commun.*, 2017, **8**, 14542.
140 D. Devasia, A. J. Wilson, J. Heo, V. Mohan and P. K. Jain, *Nat. Commun.*, 2021, **12**, 2612.
141 C. Zhan, J. Yi, S. Hu, X.-G. Zhang, D.-Y. Wu and Z.-Q. Tian, *Nat. Rev. Methods Primers*, 2023, **3**, 12.
142 C. Zhan, B.-W. Liu, Y.-F. Huang, S. Hu, B. Ren, M. Moskovits and Z.-Q. Tian, *Nat. Commun.*, 2019, **10**, 2671.
143 Y. Kuramochi, O. Ishitani and H. Ishida, *Coord. Chem. Rev.*, 2018, **373**, 333–356.
144 Y. Yamazaki, H. Takeda and O. Ishitani, *J. Photochem. Photobiol., C*, 2015, **25**, 106–137.
145 A. Perazio, G. Lowe, R. Gobetto, J. Bonin and M. Robert, *Coord. Chem. Rev.*, 2021, **443**, 214018.
146 J. Agarwal, E. Fujita, H. F. Schaefer III and J. T. Muckerman, *J. Am. Chem. Soc.*, 2012, **134**, 5180–5186.
147 Y. Hayashi, S. Kita, B. S. Brunschwig and E. Fujita, *J. Am. Chem. Soc.*, 2003, **125**, 11976–11987.
148 B. P. Sullivan, C. M. Bolinger, D. Conrad, W. J. Vining and T. J. Meyer, *J. Chem. Soc., Chem. Commun.*, 1985, 1414–1416, DOI: **10.1039/C39850001414**.
149 A. J. Morris, G. J. Meyer and E. Fujita, *Acc. Chem. Res.*, 2009, **42**, 1983–1994.
150 H. Kumagai, Y. Tamaki and O. Ishitani, *Acc. Chem. Res.*, 2022, **55**, 978–990.
151 J. Albero, Y. Peng and H. García, *ACS Catal.*, 2020, **10**, 5734–5749.
152 J. H. Jo, S. Choi, H.-Y. Cheong, J. Y. Shin, C. H. Kim, D. W. Cho, H.-J. Son, C. Pac and S. O. Kang, *Chem. –Eur. J.*, 2020, **26**, 16733–16754.
153 S.-J. Woo, S. Choi, S.-Y. Kim, P. S. Kim, J. H. Jo, C. H. Kim, H.-J. Son, C. Pac and S. O. Kang, *ACS Catal.*, 2019, **9**, 2580–2593.
154 R. R. Rodrigues, C. M. Boudreaux, E. T. Papish and J. H. Delcamp, *ACS Appl. Energy Mater.*, 2019, **2**, 37–46.
155 M. Bourrez, F. Molton, S. Chardon-Noblat and A. Deronzier, *Angew. Chem., Int. Ed.*, 2011, **50**, 9903–9906.
156 Y. Kuramochi, J. Itabashi, K. Fukaya, A. Enomoto, M. Yoshida and H. Ishida, *Chem. Sci.*, 2015, **6**, 3063–3074.
157 K. E. Dalle, J. Warnan, J. J. Leung, B. Reuillard, I. S. Karmel and E. Reisner, *Chem. Rev.*, 2019, **119**, 2752–2875.
158 S. Chardon-Noblat, A. Deronzier, R. Ziessel and D. Zsoldos, *J. Electroanal. Chem.*, 1998, **444**, 253–260.
159 M.-N. Collomb-Dunand-Sauthier, A. Deronzier and R. Ziessel, *J. Chem. Soc., Chem. Commun.*, 1994, 189–191, DOI: **10.1039/C39940000189**.
160 M. S. Choe, S. Choi, S.-Y. Kim, C. Back, D. Lee, H. S. Lee, C. H. Kim, H.-J. Son and S. O. Kang, *Inorg. Chem.*, 2021, **60**, 10235–10248.
161 J.-S. Lee, D.-I. Won, W.-J. Jung, H.-J. Son, C. Pac and S. O. Kang, *Angew. Chem., Int. Ed.*, 2017, **56**, 976–980.
162 D. Lee, S. Choi, M. S. Choe, S.-Y. Kim, K. Park, C. H. Kim, H.-J. Son and S. O. Kang, *Organometallics*, 2021, **40**, 2430–2442.
163 R. T. Hannagan, G. Giannakakis, M. Flytzani-Stephanopoulos and E. C. H. Sykes, *Chem. Rev.*, 2020, **120**, 12044–12088.
164 M. T. Darby, M. Stamatakis, A. Michaelides and E. C. H. Sykes, *J. Phys. Chem. Lett.*, 2018, **9**, 5636–5646.
165 G. Sun, Z.-J. Zhao, R. Mu, S. Zha, L. Li, S. Chen, K. Zang, J. Luo, Z. Li, S. C. Purdy, A. J. Kropf, J. T. Miller, L. Zeng and J. Gong, *Nat. Commun.*, 2018, **9**, 4454.
166 X. Zhang, G. Cui, H. Feng, L. Chen, H. Wang, B. Wang, X. Zhang, L. Zheng, S. Hong and M. Wei, *Nat. Commun.*, 2019, **10**, 5812.
167 C.-X. Zhao, J.-N. Liu, B.-Q. Li, D. Ren, X. Chen, J. Yu and Q. Zhang, *Adv. Funct. Mater.*, 2020, **30**, 2003619.
168 J. Li, H. Zeng, X. Dong, Y. Ding, S. Hu, R. Zhang, Y. Dai, P. Cui, Z. Xiao, D. Zhao, L. Zhou, T. Zheng, J. Xiao, J. Zeng and C. Xia, *Nat. Commun.*, 2023, **14**, 340.
169 B. H. Ko, B. Hasa, H. Shin, E. Jeng, S. Overa, W. Chen and F. Jiao, *Nat. Commun.*, 2020, **11**, 5856.
170 J. Wang, H.-Y. Tan, Y. Zhu, H. Chu and H. M. Chen, *Angew. Chem., Int. Ed.*, 2021, **60**, 17254–17267.
171 Y. Zhao, X. Chang, A. S. Malkani, X. Yang, L. Thompson, F. Jiao and B. Xu, *J. Am. Chem. Soc.*, 2020, **142**, 9735–9743.
172 X. Zhi, Y. Jiao, Y. Zheng, A. Vasileff and S.-Z. Qiao, *Nano Energy*, 2020, **71**, 104601.
173 W. Wu, J. Long and J. Xiao, *ChemCatChem*, 2025, **17**, e202401785.
174 S. Rasul, D. H. Anjum, A. Jedidi, Y. Minenkov, L. Cavallo and K. Takanabe, *Angew. Chem., Int. Ed.*, 2015, **54**, 2146–2150.
175 S. Sarfraz, A. T. Garcia-Esparza, A. Jedidi, L. Cavallo and K. Takanabe, *ACS Catal.*, 2016, **6**, 2842–2851.
176 A. Vasileff, C. Xu, L. Ge, Y. Zheng and S.-Z. Qiao, *Chem. Commun.*, 2018, **54**, 13965–13968.
177 A. Vasileff, X. Zhi, C. Xu, L. Ge, Y. Jiao, Y. Zheng and S.-Z. Qiao, *ACS Catal.*, 2019, **9**, 9411–9417.
178 X. Guo, Y. Zhang, C. Deng, X. Li, Y. Xue, Y.-M. Yan and K. Sun, *Chem. Commun.*, 2015, **51**, 1345–1348.
179 S. Ma, M. Sadakiyo, M. Heima, R. Luo, R. T. Haasch, J. I. Gold, M. Yamauchi and P. J. A. Kenis, *J. Am. Chem. Soc.*, 2017, **139**, 47–50.
180 F. Jia, X. Yu and L. Zhang, *J. Power Sources*, 2014, **252**, 85–89.
181 J. Monzó, Y. Malewski, R. Kortlever, F. J. Vidal-Iglesias, J. Solla-Gullón, M. T. M. Koper and P. Rodriguez, *J. Mater. Chem. A*, 2015, **3**, 23690–23698.
182 Z. Zhao and G. Lu, *J. Phys. Chem. C*, 2019, **123**, 4380–4387.
183 C. Wang, M. Cao, X. Jiang, M. Wang and Y. Shen, *Electrochim. Acta*, 2018, **271**, 544–550.
184 K. Ye, A. Cao, J. Shao, G. Wang, R. Si, N. Ta, J. Xiao and G. Wang, *Sci. Bull.*, 2020, **65**, 711–719.
185 V. A. Kislenko, S. A. Kislenko and V. A. Nikitina, *J. Electroanal. Chem.*, 2024, **975**, 118718.
186 X. Yu, Y. Xu, L. Li, M. Zhang, W. Qin, F. Che and M. Zhong, *Nat. Commun.*, 2024, **15**, 1711.
187 Y. Morikawa, K. Iwata and K. Terakura, *Appl. Surf. Sci.*, 2001, **169–170**, 11–15.
188 H. Wang, N. Zhang, H.-Y. Ma and X. Chen, *ACS Appl. Nano Mater.*, 2024, **7**, 21717–21727.

189 T. Zheng, C. Liu, C. Guo, M. Zhang, X. Li, Q. Jiang, W. Xue, H. Li, A. Li, C.-W. Pao, J. Xiao, C. Xia and J. Zeng, *Nat. Nanotechnol.*, 2021, **16**, 1386–1393.

190 Y. Zhong, X. Kong, Z. Song, Y. Liu, L. Peng, L. Zhang, X. Luo, J. Zeng and Z. Geng, *Nano Lett.*, 2022, **22**, 2554–2560.

191 G. Kyriakou, M. B. Boucher, A. D. Jewell, E. A. Lewis, T. J. Lawton, A. E. Baber, H. L. Tierney, M. Flytzani-Stephanopoulos and E. C. H. Sykes, *Science*, 2012, **335**, 1209–1212.

192 J. Zhang, C. Guo, S. Fang, X. Zhao, L. Li, H. Jiang, Z. Liu, Z. Fan, W. Xu, J. Xiao and M. Zhong, *Nat. Commun.*, 2023, **14**, 1298.

193 A. J. Welch, J. S. DuChene, G. Tagliabue, A. Davoyan, W.-H. Cheng and H. A. Atwater, *ACS Appl. Energy Mater.*, 2019, **2**, 164–170.

194 W. Zhu, Y.-J. Zhang, H. Zhang, H. Lv, Q. Li, R. Michalsky, A. A. Peterson and S. Sun, *J. Am. Chem. Soc.*, 2014, **136**, 16132–16135.

195 B. Kim, S. Ma, H.-R. Molly Jhong and P. J. A. Kenis, *Electrochim. Acta*, 2015, **166**, 271–276.

196 T. Hatsukade, K. P. Kuhl, E. R. Cave, D. N. Abram and T. F. Jaramillo, *Phys. Chem. Chem. Phys.*, 2014, **16**, 13814–13819.

197 Z. Geng, X. Kong, W. Chen, H. Su, Y. Liu, F. Cai, G. Wang and J. Zeng, *Angew. Chem., Int. Ed.*, 2018, **57**, 6054–6059.

198 H. Wang, X. Zhou, T. Yu, X. Lu, L. Qian, P. Liu and P. Lei, *Electrochim. Acta*, 2022, **426**, 140774.

199 Y. Hori, H. Wakebe, T. Tsukamoto and O. Koga, *Electrochim. Acta*, 1994, **39**, 1833–1839.

200 Y. Wang, X. Cui, J. Zhang, J. Qiao, H. Huang, J. Shi and G. Wang, *Prog. Mater. Sci.*, 2022, **128**, 100964.

201 K. Liu, J. Li, Y. Liu, M. Wang and H. Cui, *J. Energy Chem.*, 2023, **79**, 515–534.

202 J. Hu, F. Yang, J. Qu, Y. Cai, X. Yang and C. M. Li, *J. Energy Chem.*, 2023, **87**, 162–191.

203 H. Liu, H. Rong and J. Zhang, *ChemSusChem*, 2022, **15**, e202200498.

204 Y. Chen, J. Lin, Q. Pan, X. Liu, T. Ma and X. Wang, *Angew. Chem., Int. Ed.*, 2023, **62**, e202306469.

205 Y. Hu, Z. Li, B. Li and C. Yu, *Small*, 2022, **18**, 2203589.

206 X. Zhao, K. Zhao, Y. Liu, Y. Su, S. Chen, H. Yu and X. Quan, *ACS Catal.*, 2022, **12**, 11412–11420.

207 J. Wang, E. Kim, D. P. Kumar, A. P. Rangappa, Y. Kim, Y. Zhang and T. K. Kim, *Angew. Chem., Int. Ed.*, 2022, **61**, e202113044.

208 B. Deng, M. Huang, X. Zhao, S. Mou and F. Dong, *ACS Catal.*, 2022, **12**, 331–362.

209 Z. Yuan, X. Zhu, X. Gao, C. An, Z. Wang, C. Zuo, D. D. Dionysiou, H. He and Z. Jiang, *Environ. Sci. Ecotechnology*, 2024, **20**, 100368.

210 M. Favaro, H. Xiao, T. Cheng, W. A. Goddard, J. Yano and E. J. Crumlin, *Proc. Natl. Acad. Sci. U. S. A.*, 2017, **114**, 6706–6711.

211 Y. Li, S. Li and H. Huang, *Chem. Eng. J.*, 2023, **457**, 141179.

212 X. Fu, T. Ren, S. Jiao, Z. Tian, J. Yang and Q. Li, *J. Energy Chem.*, 2023, **83**, 397–422.

213 X. Chang, T. Wang and J. Gong, *Energy Environ. Sci.*, 2016, **9**, 2177–2196.

214 Y. Yang, Z. Tan, J. Zhang, J. Yang, R. Zhang, S. Wang, Y. Song and Z. Su, *Green Energy Environ.*, 2024, **9**, 1459–1465.

215 W. Lee, Y. E. Kim, M. H. Youn, S. K. Jeong and K. T. Park, *Angew. Chem., Int. Ed.*, 2018, **57**, 6883–6887.

216 J.-J. Lv, R. Yin, L. Zhou, J. Li, R. Kikas, T. Xu, Z.-J. Wang, H. Jin, X. Wang and S. Wang, *Angew. Chem., Int. Ed.*, 2022, **61**, e202207252.

217 J. Fu, K. Jiang, X. Qiu, J. Yu and M. Liu, *Mater. Today*, 2020, **32**, 222–243.

218 J. Zhang, J. Jiang, Y. Lei, H. Liu, X. Tang, H. Yi, X. Huang, S. Zhao, Y. Zhou and F. Gao, *Sep. Purif. Technol.*, 2024, **328**, 125056.

219 J. Lee, O. K. Farha, J. Roberts, K. A. Scheidt, S. T. Nguyen and J. T. Hupp, *Chem. Soc. Rev.*, 2009, **38**, 1450–1459.

220 N. Stock and S. Biswas, *Chem. Rev.*, 2012, **112**, 933–969.

221 W. Lu, Z. Wei, Z.-Y. Gu, T.-F. Liu, J. Park, J. Park, J. Tian, M. Zhang, Q. Zhang, T. Gentle Iii, M. Bosch and H.-C. Zhou, *Chem. Soc. Rev.*, 2014, **43**, 5561–5593.

222 K. Khaletskaya, A. Pougin, R. Medishetty, C. Rösler, C. Wiktor, J. Strunk and R. A. Fischer, *Chem. Mater.*, 2015, **27**, 7248–7257.

223 X. Li and Q.-L. Zhu, *EnergyChem*, 2020, **2**, 100033.

224 X.-F. Yang, A. Wang, B. Qiao, J. Li, J. Liu and T. Zhang, *Acc. Chem. Res.*, 2013, **46**, 1740–1748.

225 J.-M. Huang, X.-D. Zhang, J.-Y. Huang, D.-S. Zheng, M. Xu and Z.-Y. Gu, *Coord. Chem. Rev.*, 2023, **494**, 215333.

226 Y. Zhao, L. Zheng, D. Jiang, W. Xia, X. Xu, Y. Yamauchi, J. Ge and J. Tang, *Small*, 2021, **17**, 2006590.

227 J. Wang, Y. Zhang, Y. Ma, J. Yin, Y. Wang and Z. Fan, *ACS Mater. Lett.*, 2022, **4**, 2058–2079.

228 D. Li, M. Kassymova, X. Cai, S.-Q. Zang and H.-L. Jiang, *Coord. Chem. Rev.*, 2020, **412**, 213262.

229 H. Zhang, J. Li, Q. Tan, L. Lu, Z. Wang and G. Wu, *Chem. – Eur. J.*, 2018, **24**, 18137–18157.

230 A. M. Appel, J. E. Bercaw, A. B. Bocarsly, H. Dobbek, D. L. DuBois, M. Dupuis, J. G. Ferry, E. Fujita, R. Hille, P. J. A. Kenis, C. A. Kerfeld, R. H. Morris, C. H. F. Peden, A. R. Portis, S. W. Ragsdale, T. B. Rauchfuss, J. N. H. Reek, L. C. Seefeldt, R. K. Thauer and G. L. Waldrop, *Chem. Rev.*, 2013, **113**, 6621–6658.

231 S. Kreft, D. Wei, H. Junge and M. Beller, *EnergyChem*, 2020, **2**, 100044.

232 D. Li, K. Yang, J. Lian, J. Yan and S. Liu, *Adv. Energy Mater.*, 2022, **12**, 2201070.

233 Y. Wang, P. Han, X. Lv, L. Zhang and G. Zheng, *Joule*, 2018, **2**, 2551–2582.

234 W. Zhang, Y. Hu, L. Ma, G. Zhu, Y. Wang, X. Xue, R. Chen, S. Yang and Z. Jin, *Adv. Sci.*, 2018, **5**, 1700275.

235 F. Pan and Y. Yang, *Energy Environ. Sci.*, 2020, **13**, 2275–2309.

236 Y. Y. Birdja, E. Pérez-Gallent, M. C. Figueiredo, A. J. Göttle, F. Calle-Vallejo and M. T. M. Koper, *Nat. Energy*, 2019, **4**, 732–745.

237 A. Vasileff, C. Xu, Y. Jiao, Y. Zheng and S.-Z. Qiao, *Chem*, 2018, **4**, 1809–1831.
238 J. Ran, M. Jaroniec and S.-Z. Qiao, *Adv. Mater. Lett.*, 2018, **30**, 1704649.
239 S. Bai, J. Jiang, Q. Zhang and Y. Xiong, *Chem. Soc. Rev.*, 2015, **44**, 2893–2939.
240 A. Mills and S. Le Hunte, *J. Photochem. Photobiol., A*, 1997, **108**, 1–35.
241 L. Jiang, X. Yuan, Y. Pan, J. Liang, G. Zeng, Z. Wu and H. Wang, *Appl. Catal., B*, 2017, **217**, 388–406.
242 S. Li, K. Ji, M. Zhang, C. He, J. Wang and Z. Li, *Nanoscale*, 2020, **12**, 9533–9540.
243 D. Li and H. Haneda, *Chemosphere*, 2003, **51**, 129–137.
244 S. Xie, W. Ma, X. Wu, H. Zhang, Q. Zhang, Y. Wang and Y. Wang, *Energy Environ. Sci.*, 2021, **14**, 37–89.
245 J. Xiong, J. Di, J. Xia, W. Zhu and H. Li, *Adv. Funct. Mater.*, 2018, **28**, 1801983.